

**Remote sensing of the absorption coefficients and chlorophyll *a* concentration in the
U.S. southern Middle Atlantic Bight from SeaWiFS and MODIS-Aqua**

Xiaoju Pan¹, Antonio Mannino¹, Mary E. Russ^{1,2}, Stanford B. Hooker¹

¹NASA Goddard Space Flight Center, Greenbelt, Maryland, USA

²University of Maryland, Baltimore County, Goddard Earth Sciences and Technology
Center

Accepted by the Journal of Geophysical Research – Oceans September 2008

Index terms:

0480 Remote sensing

0422 Bio-optics

4219 Continental shelf and slope processes

4805 Biogeochemical cycles, processes, and modeling

Key Words: absorption, chlorophyll, remote sensing, SMAB, SeaWiFS, MODIS

Corresponding Author:

Xiaoju Pan

NASA Goddard Space Flight Center, Mail Code 614.7, Build 22 Room 248

Greenbelt, Maryland 20771, USA

Phone: +1 301 286 8966

FAX: +1 301 286 5337

E-mail: xpan@neptune-web.gsfc.nasa.gov

1 Abstract

2 At present, satellite remote sensing of coastal water quality and constituent
3 concentration is subject to large errors as compared to the capability of satellite sensors in
4 oceanic waters. In this study, field measurements collected on a series of cruises within
5 U.S. southern Middle Atlantic Bight (SMAB) were applied to improve retrievals of
6 satellite ocean color products in order to examine the factors that regulate the bio-optical
7 properties within the continental shelf waters of the SMAB. The first objective was to
8 develop improvements in satellite retrievals of absorption coefficients of phytoplankton
9 (a_{ph}), colored dissolved organic matter (CDOM) (a_g), non-pigmented particles (a_d), and
10 non-pigmented particles plus CDOM (a_{dg}), and chlorophyll *a* concentration ([Chl_a]).
11 Several algorithms were compared to derive constituent absorption coefficients from
12 remote sensing reflectance (R_{rs}) ratios. The validation match-ups showed that the mean
13 absolute percent differences (MAPD) were typically <35%, although higher errors were
14 found for a_d retrievals. Seasonal and spatial variability of satellite-derived absorption
15 coefficients and [Chl_a] was apparent and consistent with field data. CDOM is a major
16 contributor to the bio-optical properties of the SMAB, accounting for 35-70% of total
17 light absorption by particles plus CDOM at 443 nm, as compared to 30-45% for
18 phytoplankton and 0-20% for non-pigmented particles. The overestimation of [Chl_a]
19 from the operational satellite algorithms may be attributed to the strong CDOM
20 absorption in this region. River discharge is important in controlling the bio-optical
21 environment, but cannot explain all of the regional and seasonal variability of
22 biogeochemical constituents in the SMAB.

1 1. Introduction

2 Satellites such as the Sea-viewing Wide Field-of-view Sensor (SeaWiFS) and the
3 MODerate-resolution Imaging Spectrometer (MODIS) have been widely applied to the
4 study of biogeochemical processes [IOCCG, 1999; McClain *et al.*, 2004]. Based on bio-
5 optical theory, the satellite measurement, here remote sensing reflectance (R_{rs}), is often
6 related to inherent optical properties (IOPs) such as the absorption coefficient (a) and
7 scattering coefficient (b) [Garver and Siegel, 1997; Gordon *et al.*, 1988; Kirk, 1994;
8 Maritorena *et al.*, 2002; Mobley, 1994]. IOPs are often related to relevant
9 biogeochemical constituents such as chlorophyll *a* concentration ([Chl_ *a*]), dissolved
10 organic carbon (DOC), particulate organic carbon (POC), and suspended sediment
11 [Ferrari *et al.*, 2003; Mannino *et al.*, 2008; Rochelle-Newall and Fisher, 2002; Siegel *et*
12 *al.*, 2002].

13 Although chlorophyll *a* pigment plays a critical role in understanding the bio-
14 optical properties in oceanic waters, it is insufficient to fully characterize the
15 biogeochemical properties, especially in coastal waters where colored dissolved organic
16 matter (CDOM) and sedimentary resuspended matter often overwhelm phytoplankton in
17 the contribution to bio-optical properties [Gordon and Morel, 1983; IOCCG, 2006; Kirk,
18 1994; Mobley, 1994]. In general, IOPs are composed of four components: pure water,
19 phytoplankton, CDOM, and non-pigmented particles [Kirk, 1994; Mobley, 1994].

20 Absorption from components other than pure water is often considered to be strongly
21 correlated to [Chl_ *a*] in oceanic Case 1 waters, while such an assumption often breaks
22 down in Case 2 waters (e.g. coastal and inland waters) [Gordon and Morel, 1983;
23 IOCCG, 2000; Kirk, 1994; Mobley, 1994].

1 In theory semi-analytic (SA) models, which apply spectral deconvolution, are
2 applicable to retrieve constituent IOPs from R_{rs} [IOCCG, 2006]. For instance, the GSM01
3 model [Garver and Siegel, 1997; Maritorena *et al.*, 2002] produces [Chl_a], absorption
4 coefficient of CDOM and non-pigmented particles (a_{dg}), and particulate backscattering
5 coefficient (b_{bp}). Unfortunately there are at least two problems with SA models applied to
6 coastal waters. First, SA models require detailed knowledge of IOP relationships, which
7 vary regionally or seasonally in coastal waters and in fact are regionally specific or
8 empirically derived [Babin *et al.*, 2003a, 2003b; Magnuson *et al.*, 2004]. Second, SA
9 models are equally sensitive to signals at all wavelengths and require them to be equally
10 accurate. In coastal waters the satellite-derived water-leaving radiances (L_w) at shorter
11 wavelengths (e.g. 412 and 443 nm) often contain some error. Incorrect atmospheric
12 correction due to inadequate information on aerosol absorption and the selection of
13 inappropriate aerosol model, along with the weak signal-to-noise ratio due to strong
14 CDOM absorption, often causes errors on L_w derivation in coastal waters [Bailey and
15 Werdell, 2006; IOCCG, 2000; Siegel *et al.*, 2000, 2005]. Consequently, the application of
16 SA models in coastal waters faces a significant challenge because of the requirement of
17 highly accurate L_w at all wavelengths.

18 Empirical algorithms do not require a full understanding of fundamental bio-
19 optical theory. For example, they provide a direct link between satellite-sensed radiance
20 and relevant bio-optical parameters such as [Chl_a] and diffuse attenuation coefficient
21 (K_d) on global and regional scales [Harding *et al.*, 2005; Mueller, 2000; O'Reilly *et al.*,
22 1998, 2000; Signorini *et al.*, 2005]. The creation of empirical algorithms, however,
23 requires a sufficient size of highly accurate field measurements spanning all seasons and

adequate spatial coverage for the regions of interest. Thus, empirical algorithms are subject to updates as the dataset increases in size. In the work presented here, a set of self-consistent field R_{rs} data is applied to derive absorption coefficients of oceanic constituents in the U.S. southern Middle Atlantic Bight (SMAB). Absorption coefficients are very important bio-optical properties in the study of radiative transfer modeling and heat budget [Mobley, 1994], carbon flux (e.g. [Chl_a], primary production, DOC, and POC) [Arrigo and Brown, 1996; Behrenfeld et al., 2005; IOCCG, 2006; Mannino et al., 2008; Marra et al., 2007; Rochelle-Newall and Fisher, 2002], water quality (e.g. diffuse attenuation coefficient) [Mueller, 2000], and oceanic physical processes (e.g. salinity distribution) [Rochelle-Newall and Fisher, 2002]. The objectives of this work were: 1) to develop and validate satellite algorithms in deriving constituent absorption coefficients for phytoplankton, non-pigmented particles, and CDOM and [Chl_a] near the ocean surface within the SMAB to within $\pm 35\%$ uncertainty, 2) to determine the relative importance of phytoplankton, CDOM, and detritus in sunlight absorption, and 3) to evaluate the seasonal and regional impacts of river discharge on biogeochemical constituents in the SMAB.

2. Methods

2.1. Study region and field experiments

This study focuses on the SMAB from the Delaware Bay (DB) mouth to the region south of the Chesapeake Bay (CB) mouth (Figure 1). This region is well recognized for the significant impacts by riverine discharge from the Delaware and Chesapeake Bays, which account for most of the salinity variability of the SMAB [Acker

1 *et al.*, 2005; *Austin*, 2002; *Harding*, 1994]. The magnitude of freshwater run-off, along
2 with wind and tidal forcing, generates periodic outflow plumes (e.g. winter-spring plume
3 and fall sub-plume) for this region, and enhances the bio-optical complexity of the
4 SMAB compared to pelagic regions of the Atlantic Ocean [*Acker et al.*, 2005; *Harding*,
5 1994; *Johnson*, 2001; *O'Reilly and Zetlin*, 1998; *Rennie et al.*, 1999].

6 Multiple cruises were conducted in this region during 2004-2006, including the
7 Bio-physical Interactions in Ocean Margin Ecosystems cruises (BIOME) during 30
8 March to 1 April 2005 (BIOME1), 26 to 30 July 2005 (BIOME2), 9 to 12 May 2006
9 (BIOME3), and 2 to 6 July 2006 (BIOME4), and the Chesapeake Bay Plume cruises
10 (CBP) during 27 May and 3 November 2005, and 6 September and 28 November 2006,
11 and the Chesapeake Bay Hydrological survey (CBH) during 5 May, 5 July, 1 September,
12 15 October, and 15 November 2004, and 10 January, 26 May, 21 June, 19 August, and 23
13 September 2005 (Figure 1). The collected bio-optical data included, but not limited to,
14 phytoplankton pigments, IOPs (absorption), and R_{rs} (only on BIOME and CBP cruises in
15 2005). Water samples were collected at multiple depths with Niskin bottles.

17 2.2. Pigments and absorption coefficient

18 Pigment samples were collected on 25 mm GF/F filters under a gentle vacuum
19 (<5 in Hg) and stored in liquid nitrogen in the field before transfer to a -80°C freezer in
20 the laboratory. Pigments were analyzed at Horn Point Laboratory by reverse-phase high-
21 performance liquid chromatography (HPLC) with a C8 column on the HPLC system
22 equipped with photodiode array detector [*Van Heukelem and Thomas*, 2001]. [Chl_a]

1 was calculated as the sum of concentration from monovinyl Chl_a, divinyl Chl_a, and
2 chlorophyllide *a*.

3 Absorption coefficients of particles (a_p) and non-pigmented particles (a_d) were
4 determined by the quantitative “filter pad” method following the recommendations of
5 *Mitchell et al.* [2002]. Particulate samples were collected on 25 mm GF/F filters under a
6 gentle vacuum (<5 in Hg) and stored in liquid nitrogen in the field before transfer to a -
7 80°C freezer in the laboratory. Non-pigmented particulate samples were defined as the
8 detritus component of particulate samples after two cold methanol extractions (first 5 ml
9 for 10 minutes, then 10 ml for 1 hour) [*Kishino et al.*, 1985]. Artificial seawater pre-
10 filtered through 0.2 µm Whatman Nuclepore filters was used to rinse off methanol and to
11 hydrate the GF/F filters of both blanks and samples. CDOM samples were collected by
12 filtering seawater through pre-combusted (6 hours at 450°C) GF/F filters and stored
13 under refrigeration (4 to 8 °C). In the laboratory, CDOM samples were warmed to room
14 temperature and filtered through 0.2 µm Whatman Nuclepore (polycarbonate) or Gelman
15 Supor (polyethersulfone) filters prior to analysis [*Mannino et al.*, 2008].

16 Absorbance spectra were measured using a double-beam Cary 100 Bio
17 Ultraviolet-Visible scanning spectrophotometer through 250-800 nm (CDOM in Suprasil
18 quartz 10 cm pathlength cells) or 300-800 nm (particles) in 1 nm intervals. Blank GF/F
19 filters hydrated with 0.2 µm pre-filtered artificial seawater and ultraviolet (UV) oxidized
20 Milli-Q water were used as the blank and reference for particulate absorbance and
21 CDOM absorbance, respectively. Null correction was made by subtracting the mean of
22 absorbance at 790 to 800 nm for particulate samples for each spectrum. No null
23 correction for CDOM absorption was made since the raw absorbance of seawater samples

at 690-700 nm was within the noise level of the instrument [Mannino *et al.*, 2008]. The multiple-scattering effect for calculating particulate absorption coefficient (a_p) and non-pigmented particulate absorption coefficient (a_d) was corrected following the method of Mitchell [1990], from which non-pigmented particulate samples were assumed to have the same multiple-scattering amplification factor to total particulate samples [Mitchell *et al.*, 2002]. Phytoplankton absorption coefficient (a_{ph}) was calculated as $a_{ph} = a_p - a_d$. The absorption coefficient by CDOM and non-pigmented particles (a_{dg}) was calculated as the sum of a_d and CDOM absorption coefficient (a_g). Total absorption coefficient (a) was calculated as $a = a_w + a_p + a_g$, where pure water absorption coefficient (a_w) was adopted from Pope and Fry [1997].

The absorption coefficient from non-pigmented particles, CDOM, or their sum (a_x) was fitted to an exponential function as:

$$a_x(\lambda) = a_x(\lambda_0) \exp[-S_x(\lambda - \lambda_0)] \quad (1)$$

Here, S_x represents the exponential slope for absorption coefficient from non-pigmented particles (S_d), CDOM (S_g), or their sum (S_{dg}). We selected the reference wavelength, λ_0 , equal to 380 nm. In Equation (1), the wavelengths analyzed were 350 to 600 nm for $a_g(\lambda)$, and 380 to 730 nm for $a_d(\lambda)$ but excluding 400 to 480 nm and 620 to 710 nm to avoid the chlorophyll pigment peaks due to methanol's incapability to extract some pigments as discussed by Jeffrey *et al.* [1997], and 380 to 600 nm (but excluding 400 to 480 nm) for $a_{dg}(\lambda)$ [Babin *et al.*, 2003b].

The phytoplankton absorption coefficient (a_{ph}) is typically related to [Chl_a] as a power function [Bricaud *et al.*, 1995, 1998; Prieur and Sathyendranath, 1981]:

$$a_{ph}(\lambda) = A_0(\lambda)[Chl_a]^{A_1(\lambda)} \quad (2)$$

The modification of Equation (2) provides an expression of a_{ph} from its value at a reference wavelength (here 670 nm):

$$a_{ph}(\lambda) = B_0(\lambda)[a_{ph}(670)]^{B_1(\lambda)} \quad (3)$$

$A_i(\lambda)$ and $B_i(\lambda)$ are derived coefficients. [Chl_a] can also be determined from $a_{ph}(670)$ by a power function similar to Equation (3).

2.3. Apparent optical properties from *in situ* measurements

The remote sensing reflectance (R_{rs}) spectra (bands centered at 320, 340, 380, 395, 412, 443, 465, 490, 510, 532, 555, 560, 625, 665, 670, 683, 710, 780, and 860 nm, and each band is 10 nm wide at full-width half max) were determined with a BioPro in-water profiling spectroradiometer (Biospherical Instruments, Inc., San Diego, CA), as described in detail by Mannino *et al.* [2008]. The instrument was deployed multiple times for each station, and the absolute uncertainty was less than 5%. The R_{rs} at 551 nm was calculated from a linear interpolation of values at 532, 555, and 560 nm [Mannino *et al.*, 2008]. The R_{rs} at 488 nm was assumed to be equivalent to the value at 490 nm. R_{rs} measured at 6 stations during BIOME1 cruise, 19 stations during BIOME2 cruise, and 3

1 and 6 stations during CBP cruises on 27 May and 3 November 2005 were included for
2 analysis in this paper.

3 4 2.4. Satellite ocean color validation

5 The method to process satellite images was described in *Mannino et al.* [2008]
6 following *Bailey and Werdell* [2006] protocols. SeaWiFS and MODIS-Aqua observations
7 were processed from Level 1 to Level 2 using the SeaWiFS Data Analysis System
8 software (SeaDAS version 5.1.1 and ms12 version 5.6.3). The pixels were masked after
9 atmospheric correction by any of the following flags: land, cloud or ice, high top-of-
10 atmosphere radiance, low normalized water-leaving radiance at 551 or 555 nm, stray
11 light, sun glint, or atmospheric correction failure) [*Bailey and Werdell*, 2006]. Pixels with
12 $L_w(412) < 0.2 \text{ mW cm}^{-2} \mu\text{m}^{-1} \text{ sr}^{-1}$ were excluded to minimize the impacts from atmospheric
13 over-correction in causing negative or significantly reduced water-leaving radiance
14 [*Siegel et al.*, 2002]. The 3x3 pixel arrays centered on the field stations, each with ~1 km
15 resolution (sensor native), were analyzed. The satellite observations which occurred
16 within ± 8 hours and ± 32 hours of in situ measurements were considered for match-up
17 analysis to allow for inclusion of sufficient data points.

18 19 2.5. Analysis and validation methods

20 Three curve-fitting functions, linear function (Model II regression) after log-
21 transformation (log_linear_model; Equation 4), fourth-order polynomial function after
22 log-transformation similar to OC4V4 [*O'Reilly et al.*, 1998, 2000]
23 (log_polynomial_model; Equation 5), and one-phase exponential decay function

(exponential_model; Equation 6), were developed to correlate R_{rs} band ratio to the relevant absorption products:

$$\log[a_i(\lambda)] = C_0(\lambda) + C_1(\lambda)R \quad (4)$$

$$\log[a_i(\lambda)] = D_0(\lambda) + D_1(\lambda)R + D_2(\lambda)R^2 + D_3(\lambda)R^3 + D_4(\lambda)R^4 \quad (5)$$

$$a_i(\lambda) = G_0(\lambda) + G_1(\lambda) \exp[-G_2(\lambda) \frac{R_{rs}(\lambda_1)}{R_{rs}(\lambda_2)}] \quad (6)$$

Here, $R = \log[R_{rs}(\lambda_1)/R_{rs}(\lambda_2)]$, and λ_1 and λ_2 represent the various bands evaluated, and C_i , D_i and G_i are wavelength-specific derived coefficients, and a_i is the analyzed absorption coefficient as a_{ph} , a_d , a_g , or a_{dg} . In addition, a one-phase exponential function to determine R_{rs} from a_i similar to *Mannino et al.* [2008] was also developed, and a_i was then calculated by its reverse function (reverse_exponential_model; Equation 7):

$$\frac{R_{rs}(\lambda_1)}{R_{rs}(\lambda_2)} = H_0(\lambda) + H_1(\lambda) \exp[-H_2(\lambda)a_i(\lambda)] \quad (7)$$

Four products, $a_{ph}(670)$, $a_d(380)$, $a_g(380)$, and $a_{dg}(380)$, whose surface measurements were represented as the site values, were analyzed with the above equations. The mean absolute percent difference (MAPD) and root mean square error (RMSE) between the modeled products (C_{alg}) and field measurements (C_{field}) were calculated.

$$MAPD = \frac{\sum |(C_{alg} - C_{field}) / C_{field}|}{N} \times 100\% \quad (8)$$

$$RMSE = \sqrt{\sum (C_{alg} - C_{field})^2 / N} \quad (9)$$

2.6. Monthly time series analysis

Monthly Level 3 mapped MODIS-Aqua images (4 km resolution) from July 2002 to December 2006 were downloaded from the NASA ocean color website (<http://oceancolor.gsfc.nasa.gov>) on 8 January 2008. Empirical algorithms developed from this paper were applied to calculate products such as [Chl_a], a_{ph} , a_d , and a_g . Three stations—Location A (75.90W, 36.93N), B (75.30W, 36.93N), and C (74.77W, 36.93N) representing a transect from the Chesapeake Bay mouth to an outer shelf location—were selected and plotted to demonstrate a monthly time series.

3. Results and Discussion

3.1. Absorption spectra

We observed seasonal transitions in phytoplankton absorption coefficients in April-May and October-November periods. Therefore, at least two seasonal algorithms (May-October and November-April) are required to describe phytoplankton absorption relationships (Figure 2a and Table 1). In general, the phytoplankton absorption ratio [$a_{ph}(\lambda)/a_{ph}(670)$] in May-October is higher than that in November-April (Figure 2a). This coincides with historical observations that the dominant phytoplankton taxa are diatoms

in winter and spring, but the phytoplankton assemblage transitions to a greater proportion of dinoflagellates, cryptophytes, and cyanobacteria in summer and fall [Adolf *et al.*, 2006; Marshall and Alden, 1993]. Although phytoplankton absorption coefficients are subject to seasonal variation, the relationship between $a_{ph}(670)$ and [Chl_a] ($r^2=0.964$, $N=230$; Figure 2b) is relatively constant seasonally due to the dominant contribution from Chl_a to $a_{ph}(670)$ [Jeffrey *et al.*, 1997]:

$$[Chl_a] = 70.632 \times [a_{ph}(670)]^{1.184} \quad (10)$$

Seasonal variability of riverine discharge, along with other factors such as wind forcing and direction, may cause the seasonal variability of phytoplankton taxonomic composition, pigment package effect, and therefore normalized phytoplankton absorption spectra (Figure 2a) [Babin *et al.*, 2003b; Bricaud *et al.*, 1995, 1998; Trees *et al.*, 2000]. The pigment package effect refers to a consequence of the fact that in the natural waters pigment molecules are not uniformly distributed but are contained within discrete packages such as chloroplasts, cells, and cell colonies, which causes a flattening of the phytoplankton absorption peak due to self-shading wherever pigments are localized within cell membranes [Duysens, 1956].

Equation (1) described the exponential decay characteristics of a_d , a_g , and a_{dg} rather well with coefficients of determination (r^2) of >0.95 for a_d , and >0.99 for a_g and a_{dg} . The exponential slopes (S) covered a wide range with mean ± 1 standard deviation of 0.0122 ± 0.0023 ($N=247$, ranging from 0.0084 to 0.0260) for a_d , 0.0170 ± 0.0011 ($N=300$, ranging from 0.0137 to 0.0221) for a_g , and 0.0148 ± 0.0014 ($N=222$, ranging from 0.0122

to 0.0205) for a_{dg} . However, the general exponential decay relationships of S (ordinate) versus absorption coefficients (abscissa) for coastal regions that are significantly impacted by freshwater discharge as suggested by *Carder et al.* [1989] was not apparent for the SMAB dataset. Part of the reason was that the dataset presented in this paper (Figure 1) did not extend far into the estuaries to cover the full range of water types from freshwater to oceanic waters. The observations above suggest that using mean S values may cause significant errors in predicting a_x spectra. Multiple algorithms to retrieve a_d , a_g , and a_{dg} at multiple wavelengths may be required, as discussed in the next section.

3.2. Algorithm development and validation

Three R_{rs} band ratios (412/555, 443/555, and 490/555 for SeaWiFS, and 412/551, 443/551, and 488/551 for MODIS-Aqua) were compared to determine the best algorithm performance. No matter which of the curve-fitting models from Equations (4)-(7) was selected, algorithms based on R_{rs} band ratio at 490/555 or 488/551 performed similar to, or better than, the other two band ratios. Figure 3 shows examples of model performance on predicting $a_{ph}(670)$, $a_d(380)$, $a_g(380)$, and $a_{dg}(380)$ from Equations (4)-(7), respectively. Performance from other models, i.e. Equation (4) on predicting $a_d(380)$, $a_g(380)$, and $a_{dg}(380)$, showed similar results to Figure 3 (data not shown). Due to the possibly poor quality of satellite water-leaving radiance at shorter wavelengths (e.g. 412 and 443 nm) in coastal waters [*Bailey and Werdell, 2006; Siegel et al., 2002*], we selected R_{rs} band ratios at 490/555 or 488/551 for further analysis. Although the selection of only two bands will cause interdependence of satellite-derived products, it still provides

valuable information on bio-optical properties of the SMAB in the absence of appropriate semi-analytic algorithms based on more bands.

The `log_linear_model` (Equation 4) proved suitable to validate satellite-derived a_{ph} , a_d , and a_{dg} with relatively high r^2 and relatively low MAPD and RMSE (Figures 4-5 and Table 2). The r^2 for the `log_linear_model` ranged from 0.92 to 0.93 for all three products of $a_{ph}(670)$, $a_d(380)$, and $a_{dg}(380)$, while 0.84 to 0.95 for the other three models. The MAPD for the `log_linear_model` was typically similar to, or lower than, the other three models, regardless of the satellite sensor (SeaWiFS or MODIS-Aqua) and overpass satellite/in situ time window selected (± 8 hours or ± 32 hours) (Figures 4a-b and 5a-b). This was also supported by the validation results from the RMSE comparisons (Figures 4c-d and 5c-d). The `exponential_model` may provide lower MAPD and RMSE in some cases (Figures 4-5), but was not selected due to its relatively low r^2 (0.84 to 0.87). In contrast, the `reverse_exponential_model` yielded the best validation results for $a_g(380)$ with the highest r^2 (0.90 versus 0.77-0.86) and typically lowest MAPD and RMSE (Figures 4-5 and Table 4) as compared to the other models. *Mannino et al.* [2008] showed the same model for a_g but did not include the CBH stations in their validation analysis. The selected R_{rs} band ratio models can also be applied to derive a_d , a_g , and a_{dg} at multiple wavelengths (Tables 2-3). Except for the higher MAPD for a_d (34.8-57.5% for SeaWiFS and 41.9-65.3% for MODIS-Aqua), the selected regression methods typically limited MAPD for a_g and a_{dg} to within 30% for wavelengths between 350 and 555 nm (Table 4). The exponential decay slopes (S) for a_d , a_g , and a_{dg} can be derived from non-linear regression methods with R_{rs} band ratio models at multiple wavelengths (e.g. 355, 380, 400, 412, 443, 490, 510, 531, and 555), and agree reasonably well with field

1 derivations (Table 4). The GSM01 [Garver and Siegel, 1997; Maritorena et al., 2002]
 2 and its regional version (GSM01-CB) [Magnuson et al., 2004] resulted in relatively high
 3 MAPD and RMSE when compared with the field measurements (Figures 4-5). The
 4 GSM01 model was developed for global ocean application, and thus is not optimized for
 5 the variability of in-water constituents observed in near-shore coastal regions, such as
 6 variable or region-specific S values. However, even the optimized GSM01 model for this
 7 coastal region (GSM01-CB; primarily Chesapeake Bay and near-shore coastal ocean)
 8 developed by Magnuson et al. [2004] did not perform significantly better than GSM01,
 9 e.g. MAPD=42.6% and 46.0% for $a_{ph}(670)$ and $a_{dg}(380)$ from GSM01-CB, versus 43.3%
 10 and 40.7% from GSM01 for SeaWiFS ± 8 hour overpass window (Figures 4-5). The lack
 11 of adequate knowledge of backscattering coefficients, as well as the higher uncertainty of
 12 R_{rs} at shorter wavelengths (e.g. 412 and 443 nm) from satellite measurements, may
 13 account for the performance of GSM01 and GSM01-CB for this region [Bailey and
 14 Werdell, 2006; IOCCG, 2000; Magnuson et al., 2004; Siegel et al., 2000, 2005].

15 By applying the regression results shown in Table 1, phytoplankton absorption
 16 coefficients at other visible wavelengths can also be derived from $a_{ph}(670)$, which can be
 17 derived from satellite radiance observations as shown in Table 2. The validation match-
 18 ups based on this approach yielded similar MAPD accuracy levels for $a_{ph}(\lambda)$ at 412, 443,
 19 488, 490, 510, 667, and 678 nm to $a_{ph}(670)$ (21.5-26.1% versus 25.7% for SeaWiFS and
 20 19.0-28.1% versus 21.2% for MODIS-Aqua), but relatively higher MAPD at 531, 551,
 21 and 555 nm (27.2-30.9% for SeaWiFS and 33.1-43.1% for MODIS-Aqua) due to the
 22 relatively higher measurement errors from weaker absorption at these wavelengths (Table
 23 4). If we exclude those stations with extremely low a_{ph} (e.g. $<0.003 \text{ m}^{-1}$ at 555 nm), the

MAPD for $a_{ph}(\lambda)$ was at the same accuracy level for all visible wavelengths evaluated. The satellite derivation of [Chl_a] from Equation (10) had slightly lower but still reasonable accuracy level compared to that for $a_{ph}(670)$ with MAPD of $32.3 \pm 28.2\%$ (N=29) for SeaWiFS and $28.8 \pm 20.6\%$ (N=14) for MODIS-Aqua (Table 4).

The validation match-ups between field measurements of absorption constituents and satellite derivations within ± 8 hours demonstrated reasonable agreement (Figures 6-7). The SeaWiFS and MODIS-Aqua match-ups have similar r^2 varying from 0.80-0.97, and show slope values from 0.52 to 0.73 and from 0.46 to 0.80, respectively. Including the stations applied to develop the algorithms, which increases dataset size by 10-12 points for SeaWiFS and 5-6 points for MODIS-Aqua, yielded improvements in all the slopes (e.g. 0.73-0.87 for SeaWiFS and 0.57-0.64 for MODIS-Aqua). When extending the match-up dataset from ± 8 hours to ± 32 hours of the satellite overpass window, similar improvements were also found due to significant increase of dataset size by 50% to 140% (data not shown). The validation match-ups between field measurements of [Chl_a] and satellite derivations after log-transformation agreed well with $r^2=0.86$ to 0.95, slope=0.87 to 0.96, and RMSE=0.20 to 0.24 (Figure 7). Similar statistical results were found for $a_{ph}(670)$ when including those stations used to develop the algorithms (data not shown). It implies that these empirical algorithms are relatively successful and should improve as the size of the dataset increases.

Above all, the satellite-derived absorption coefficients from selected functions (log_linear_model for a_{ph} , a_d , and a_{dg} , and reverse_exponential_model for a_g) yielded relatively good results for the SMAB. Since the dataset used for algorithm development did not include stations from the CBH cruises (because AOP data was not collected at

those stations), the validation analyses should improve after excluding those CBH stations. For example, MAPD improved from 25.7% to 21.9% for $a_{ph}(670)$, from 35.3% to 29.5% for $a_d(380)$, from 25.2% to 20.9% for $a_g(380)$, from 26.5% to 23.8% for $a_{dg}(380)$, and from 32.3% to 24.2% for [Chl_a] for SeaWiFS ± 8 hours overpass time window. Therefore, in the future the addition of complete datasets from the lower bay locations will expand the dynamic range of the algorithms and may significantly improve the model capability in more turbid areas of the SMAB.

3.3. Seasonal variability

These empirical algorithms can be applied to study the spatial and seasonal variability of coastal ocean constituents. Figure 8 shows typical examples of the spatial distribution of the absorption coefficients within the SMAB during four seasons: summer (June-August), fall (September-November), winter (December-February), and spring (March-May). The satellite images clearly show the gradients from high to low constituent concentration between the coast and the open ocean as well as the riverine/estuarine outflow impact along the coast (Figure 8). The seasonal variability of phytoplankton absorption [e.g. $a_{ph}(443)$] may be due primarily to the river discharge rate from the bay mouths [Acker *et al.*, 2005; Adolf *et al.*, 2006; Marshall and Alden, 1993; Marshall *et al.*, 2006]. The monthly mean flow rates out of the Chesapeake Bay for these selected images were 510, 1648, 2983, and 1463 $\text{m}^3 \text{s}^{-1}$ for August 2005, November 2005, February 2006, and May 2006, respectively (Data sources: <http://waterdata.usgs.gov/nwis/>; written communication from Gary Fisher, U.S. Geological Survey, 17 July 2007). Consequently, lower phytoplankton abundance

1 occurred during the dry season in summer 2005 compared to the other three seasons. The
2 seasonal variability of detritus absorption [e.g. $a_d(443)$] is complex. At least two primary
3 sources of detritus from riverine/estuarine outflow and sedimentary resuspension
4 controlled a_d in the SMAB. The significant contribution from storm-driven sedimentary
5 resuspension in autumn may explain the higher detritus content in November 2005. The
6 seasonal variability of CDOM absorption [e.g. $a_g(443)$] may be controlled primarily by
7 the degree of riverine inputs of degraded terrestrial vegetation to the SMAB [Del Vecchio
8 and Blough, 2004; Mannino et al., 2008].

9 CDOM plays a critical role in contributing to sunlight absorption and thus impacts
10 primary production in the SMAB by reducing the amount of photosynthetically active
11 radiation (PAR) available for phytoplankton growth [Arrigo and Brown, 1996]. At 443
12 nm, CDOM accounted for 35-70% of total light absorption excluding water absorption
13 (a_{pg}), as compared to 0-20% for non-pigmented particles, and 30-45% for phytoplankton
14 (Figures 9-10). Pure seawater absorption [$a_w(443) \approx 0.007 \text{ m}^{-1}$; Pope and Fry, 1997]
15 typically accounts for a negligible fraction ($\sim 3.0\%$) of $a(443)$ in the SMAB. The
16 relatively low contribution of detritus absorption within coastal ocean regions was also
17 reported by Siegel et al. [2002] and may explain the performance of the satellite-derived
18 $a_d(\lambda)$ in the validation analysis (Table 4, and Figures 4-6). The satellite-derived $a_d(\lambda)$
19 underestimates $a_d(\lambda)$ with respect to field samples collected in the near-shore ocean
20 region ($<20 \text{ m}$ bottom depth) and overestimates $a_d(\lambda)$ in water with very low $a_d(\lambda)$
21 (Figures 6, 8, and 10). The gradients of high to low percentages of a_{ph} and a_d , and low to
22 high percentage of a_g from the coast to the open ocean were consistent with field
23 measurements (Figure 10). During the dry season (e.g. August 2005), CDOM accounts

1 for a higher percentage of total absorption than during the wet season (e.g. February 2006)
2 (Figure 9). Such a phenomenon may be explained by the impact of river discharge in
3 contributing nutrients to support phytoplankton growth as well as the export of terrestrial
4 CDOM. During the wet season, CDOM and phytoplankton abundance are both elevated,
5 but phytoplankton blooms increase the relative percentage of phytoplankton absorption
6 compared to CDOM absorption. During the dry season, CDOM and phytoplankton are
7 both low, but the reported higher primary productivity and mature grazer community may
8 result in a higher percentage of phytoplankton to be grazed and degraded which in turn
9 reduces the relative percentage of phytoplankton absorption [Adolf *et al.*, 2006; Marshall
10 and Nesius, 1996; Marshall *et al.*, 2006] and increase CDOM through grazer and
11 microbial processing of organic matter [Nelson *et al.*, 2004; Steinberg *et al.*, 2004]. Since
12 phytoplankton pigments have a much weaker relationship with CDOM absorption than
13 with phytoplankton absorption, the significant contribution of CDOM absorption may
14 pose complications for applying global operational algorithms (e.g. OC4V4 and OC3M)
15 [O'Reilly *et al.*, 1998, 2000] to coastal regions. For CDOM-rich Case 2 waters such as
16 the Chesapeake Bay, OC4V4 has been found to significantly overestimate [Chl_a],
17 especially for offshore regions of the SMAB [Harding *et al.*, 2005; Magnuson *et al.*,
18 2004]. Our results also support this conclusion. For example, match-ups within ± 8 hours
19 showed that OC4V4 performed better for the lower CB region (e.g. CBH stations) with
20 MAPD of 33.8% as compared to 79.6% for whole SMAB region (data not shown). It
21 implies that the relative difference between our approach and operational algorithms
22 would be relatively small in near-shore regions but high in offshore regions. The spatial
23 distribution and the seasonal variability of [Chl_a] based on our approach displayed

1 similar trends as those from OC4V4 and OC3M algorithms, but significantly reduced the
2 overestimation by operational Chl_a algorithms in the offshore region of the SMAB
3 (Figure 11). In general, the ratios of [Chl_a] based on operational Chl_a algorithms to our
4 approach increase with the increase of CDOM contribution to light absorption (Figures 9
5 and 11). OC4V4 and OC3M [Chl_a] were higher by 0-0.5 times for the inner-shelf
6 region, 0.4-1.2 times for the middle shelf region, and 1-2 times for the outer shelf region
7 (Figure 11). This higher ratio trend toward offshore demonstrates the impact of CDOM
8 on ocean color products in the SMAB.

9 The satellite derivations of absorption coefficients provide tools to study
10 biogeochemical processes and radiative transfer. For examples, DOC and salinity can be
11 strongly correlated to CDOM absorption [*Del Vecchio and Blough, 2004; Mannino et al.,*
12 *2008; Rochelle-Newall and Fisher, 2002*], and primary productivity is correlated to
13 phytoplankton absorption [*Behrenfeld et al., 2005; Marra et al., 2007*]. The knowledge of
14 absorption also provides methods to study other IOPs from space. For example, the
15 expression of R_{rs} from absorption and backscattering [*Garver and Siegel, 1997; Gordon*
16 *et al., 1988; Maritorena et al., 2002*] and the empirical expression of absorption from R_{rs}
17 ratio make it possible to express backscattering into R_{rs} . The knowledge of backscattering
18 might significantly improve the capability of semi-analytical models in deriving ocean
19 color products from space [*Magnuson et al., 2004*].

20 Although we have shown the significant impact of river discharge on
21 biogeochemical constituents in the SMAB, the direct link between them should be
22 interpreted with caution. First, the impact of river discharge on the coastal region of
23 Chesapeake Bay is different from Delaware Bay. The lower Chesapeake Bay is subject to

1 nutrient limitation for phytoplankton growth, in contrast to light availability in the
2 Delaware Bay [Harding *et al.*, 1986; Marshall and Alden, 1993]. Therefore, an increase
3 in river discharge is more likely to cause a phytoplankton bloom in the lower Chesapeake
4 Bay by driving more nutrients downstream, while an increase in turbidity from higher
5 river discharge may decrease primary production in the lower Delaware Bay. Second, the
6 impact of river discharge is subject to seasonal variability and distance from the bay
7 mouths, as shown in the following for the coastal region of Chesapeake Bay. In the inner-
8 shelf region, the correlation coefficients (r) between river discharge rate and
9 biogeochemical products are low (e.g. $r=0.05-0.12$ for [Chl_a] and $-0.01-0.14$ for a_g) for
10 all seasons except for summer (Figure 12). The poor correlation may be due to averaging
11 out the higher frequency responses (less than one week) for the export of nutrients and
12 CDOM, respectively, from the bays. During summer, the vertical stratification is well
13 developed [Verity *et al.*, 2002], and the strength of river discharge represents the flux of
14 nutrients for phytoplankton growth. Thus, the correlation between biogeochemical
15 products and river discharge improves for summer (e.g. $r=0.48$ for [Chl_a] and a_g)
16 (Figure 12). In the middle shelf region, however, river discharge is significantly
17 correlated to biogeochemical products in winter but poorly correlated during other
18 seasons (e.g. $r=0.79$ for [Chl_a] and a_g in winter and $r=0.09-0.36$ in other seasons)
19 (Figure 12). During winter, low water temperature and a less mature grazer community
20 may cause the phytoplankton biomass to be linked directly to nutrient availability, which
21 is driven primarily by river discharge and by wind-induced vertical mixing of nutrients
22 from depth [Adolf *et al.*, 2006; Marshall and Alden, 1993]. As the zooplankton and
23 bacterial communities develop into spring and summer, lower phytoplankton biomass

1 and higher primary productivity are expected [Adolf *et al.*, 2006] and the direct response
2 of the biological system to river discharge dissipates. The outer shelf region shows a
3 similar pattern but a lower correlation coefficient (e.g. $r=0.49$ for [Chl_a] and a_g in
4 winter, and -0.13-0.31 in other seasons) with river discharge than the middle shelf region
5 (data not shown).

6 Other physical factors than river discharge, such as water temperature and wind
7 forcing, anthropogenic activities, and even climate change, can also impact
8 phytoplankton abundance, productivity, and carbon distributions in the SMAB. For
9 example, the direction and distribution of the Chesapeake Bay plume is highly dependent
10 on the wind stress direction. During winter and early spring northerly winds
11 (downwelling favorable) and the along-shore southward current force the Chesapeake
12 Bay [Rennie *et al.*, 1999; Verity *et al.*, 2002] and Delaware Bay [Sanders and Garvine,
13 2001] plumes to flow southward along the coast. As winds reverse later in spring the
14 southerly along-shore flow weakens, and the Chesapeake Bay plume broadens and flows
15 offshore, primarily to the south and east. Upwelling-favorable conditions can initiate
16 local phytoplankton blooms and contribute additional particles to surface waters [Johnson
17 *et al.*, 2001]. The Chesapeake Bay estuarine ecosystem has experienced a large increase
18 in anthropogenic nutrient loading and reductions in the past half century which have
19 affected the floral composition and biomass [Harding, 1994; Paerl *et al.*, 2006].
20 Furthermore, climate forcing (e.g. hurricanes, drought, etc.) significantly influences
21 phytoplankton dynamics (e.g. by reducing vertical stratification, increasing sedimentary
22 resuspension, and redistributing particles from hurricane forcing) [Miller and Harding,
23 2005; Paerl *et al.*, 2006].

Above all, the impacts from physical factors (e.g. river discharge, wind forcing, and bathymetry) on bio-optical constituents (e.g. [Chl_a] and a_g) are complicated and cannot be explained by a single factor [Harding, 1994]. Nevertheless, we found that the variability of an optical property, the diffuse attenuation coefficient at 490 nm (K490), represents the variability of multiple bio-optical constituents. In the Chesapeake Bay inner-shelf site, the correlation coefficient (r) of [Chl_a], a_{ph} , a_d , a_g , and a_{dg} to K490 was 0.66-0.74, while 0.94-0.99 in the middle shelf location, and 0.93-0.98 in the outer shelf locations. These results also imply that absorption is the dominant contributor to the diffuse attenuation coefficient at offshore locations but scattering contributes significantly at near-shore locations.

4. Conclusions

Several important conclusions can be made from the present analyses of absorption coefficients and [Chl_a] derived from ocean color remote sensing. The empirical algorithms demonstrate successful retrieval of absorption coefficients and [Chl_a] within a reasonable uncertainty (e.g. $\pm 35\%$), and demonstrate significant improvements from the standard semi-analytic model (e.g. GSM01 and GSM01-CB) and operational algorithms (e.g. OC4V4 and OC3M). Field observations and satellite derivations both demonstrate that CDOM is the major contributor to water-column light absorption at shorter wavelengths (e.g. < 500 nm), especially during the dry seasons and on the outer shelf where it can account for 35-70% of absorption by particles plus CDOM at 443 nm. River discharge plays a principal role in controlling the distribution of biogeochemical constituents, but is subject to seasonal and regional variability.

1 Acknowledgements

2 This research was supported by an appointment to the NASA Postdoctoral Program at the
3 Goddard Space Flight Center, administered by Oak Ridge Associated Universities
4 through a contract with NASA. This work was funded with support from the NASA New
5 Investigator Program, Interdisciplinary Science, and Earth Observing System programs
6 and by NOAA through a grant in support of the Coastal Observatories program
7 (NA03NOS4730220). We thank the captains and crews of R/V *Cape Henlopen*, *Hugh R.*
8 *Sharp*, and *Fay Slover*. H. Throckmorton, P. Bernhardt, K. C. Filippino, C. Makinen, and
9 M. Linksweiler provided assistance in collecting particulate samples. We are grateful to
10 J. Morrow, J. Brown, D. D'Alimonte, and J.-N. Druon for deploying the profiling
11 radiometer, and L. Van Heukelem and C. Thomas for analyzing HPLC pigments, and the
12 Ocean Biology Processing Group at GSFC. J. O'Reilly kindly provided the high-
13 resolution bathymetry data.

1 References

- 2 Acker, J.G., L.W. Harding, G. Leptoukh, T. Zhu, and S. Shen (2005), Remotely-sensed
3 chl *a* at the Chesapeake Bay mouth is correlated with annual freshwater flow to
4 the Chesapeake Bay, *Geophys. Res. Lett.*, 32(L05061), doi: 10.1029/2004GL
5 021852.
- 6 Adolf, J.E., C.L. Yeager, W.D. Miller, M.E. Mallonee, and L.W. Harding (2006),
7 Environmental forcing of phytoplankton floral composition, biomass, and primary
8 productivity in Chesapeake Bay, USA, *Estuar. Coast. Shelf Sci.*, 67, 108-122.
- 9 Arrigo, K.R. and C.W. Brown (1996), Impact of chromophoric dissolved organic matter
10 on UV inhibition of primary productivity in the sea, *Mar Ecol Prog Ser.*, 140,
11 207-216.
- 12 Austin, J. (2002), Estimating the mean ocean-bay exchange rate of the Chesapeake Bay, *J.*
13 *Geophys. Res.*, 107(C11), 3192, doi: 10.1029/2001JC001246.
- 14 Babin, M., A. Morel, V. Fournier-Sicre, F. Fell, and D. Stramski (2003a), Light scattering
15 properties of marine particles in coastal and open ocean waters as related to the
16 particle mass concentration, *Limnol. Oceanogr.*, 48(2), 843-859.
- 17 Babin, M., D. Stramski, G.M. Ferrari, H. Claustre, A. Bricaud, G. Obolensky, and N.
18 Hoepffner (2003b), Variations in the light absorption coefficients of
19 phytoplankton, nonalgal particles, and dissolved organic matter in coastal waters
20 around Europe, *J. Geophys. Res.*, 108(C7), 3211, doi: 10.1029/2001JC000882.
- 21 Bailey, S.W., and P.J. Werdell (2006), A multi-sensor approach for the on-orbit
22 validation of ocean color satellite data products, *Remote Sens. Environ.*, 102, 12-
23 23.

1 Behrenfeld, M.J., E. Boss, D.A. Siegel, and D.M. Shea (2005), Carbon-based ocean
2 productivity and phytoplankton physiology from space, *Global Biogeochem.*
3 *Cycles*, 19(GB1006), doi:10.1029/2004GB002299

4 Bricaud, A., M. Babin, A. Morel, and H. Claustre (1995), Variability in the chlorophyll-
5 specific absorption coefficients in natural phytoplankton: analysis and
6 parameterization, *J. Geophys. Res.*, 100(C7), 13321-13332.

7 Bricaud, A., A. Morel, M. Babin, K. Allali, and H. Claustre (1998), Variations of light
8 absorption by suspended particles with chlorophyll a concentration in oceanic
9 (case 1) waters: analysis and implications for bio-optical models, *J. Geophys. Res.*,
10 103(C13), 31033-31044.

11 Carder, K.L., R.G. Steward, G.R. Harvey, and P.B. Ortner (1989), Marine humic and
12 fulvic acids: Their effect on remote sensing of ocean chlorophyll, *Limnol.*
13 *Oceanogr.*, 34(1), 68-81.

14 Del Vecchio, R., and N.V. Blough (2004), Spatial and seasonal distribution of
15 chromophoric dissolved organic matter (CDOM) and dissolved organic carbon
16 (DOC) in the Middle Atlantic Bight, *Mar. Chem.*, 89, 169-187.

17 Duysens, L.N.M. (1956), The flattening of the absorption spectrum of suspensions as
18 compared to that of solutions, *Biochim. Biophys. Acta*, 19, 1-12.

19 Ferrari, G.M., F.G. Bo, and M. Babin (2003), Geo-chemical and optical characterizations
20 of suspended matter in European coastal waters, *Estuar. Coast. Shelf Sci.*, 57, 17-
21 24.

1 Garver, S.A., and D.A. Siegel (1997), Inherent optical property inversion of ocean color
2 spectra and its biogeochemical interpretation: 1. Time series from the Sargasso
3 Sea, *J. Geophys. Res.*, 102(C8), 18607-18625.

4 Gordon, H.R., and A. Morel (1983), *Remote assessment of ocean color for interpretation*
5 *of satellite visible imagery*, 114 pp., Springer-Verlag, New York.

6 Gordon, H.R., O.B. Brown, R.H. Evans, J.W. Brown, R.C. Smith, K.S. Baker, and D. K.
7 Clark (1988), A semianalytic radiance model of ocean color, *J. Geophys. Res.*,
8 93(D9), 10909-10924.

9 Harding, L.W. (1994), Long-term trends in the distribution of phytoplankton in
10 Chesapeake Bay: roles of light, nutrients, and streamflow, *Mar. Ecol. Prog. Ser.*,
11 104, 267-291.

12 Harding, L., B. Mession, and T. Fisher (1986), Phytoplankton production in two east coast
13 estuaries: photosynthesis-light functions and patterns of carbon assimilation in
14 Chesapeake and Delaware Bays, *Estuar. Coast. Shelf Sci.*, 23, 773-806.

15 Harding, L.W., A. Magnuson, M.E. Mallonee (2005), SeaWiFS retrievals of chlorophyll
16 in Chesapeake Bay and the mid-Atlantic bight, *Estuar. Coast. Shelf Sci.*, 62, 75-
17 94.

18 IOCCG (1999), Status and plans for satellite ocean-colour missions: considerations for
19 complementary missions, in *Reports of the International Ocean-Color*
20 *Coordinating Group*, no. 2, edited by J. Yoder, pp. 43, Dartmouth, Nova Scotia.

21 IOCCG (2000), Remote sensing of ocean color in coastal, and optically-complex waters,
22 in *Reports of the International Ocean-Color Coordinating Group*, no. 3, edited by
23 S. Sathyendranath, pp. 140, Dartmouth, Nova Scotia.

1 IOCCG (2006), Remote sensing of inherent optical properties: Fundamentals, tests of
 2 algorithms and applicaitons, in *Reports of the International Ocean-Color*
 3 *Coordinating Group*, no. 5, edited by Z. Lee, pp. 126, Dartmouth, Nova Scotia.

4 Jeffrey, S.W., R.F.C. Mantoura, and S.W. Wright (1997), *Phytoplankton pigments in*
 5 *oceanography*, UNESCO Publishing.

6 Johnson, D.R., A. Weidemann, R. Arnone, and C.O. Davis (2001), Chesapeake Bay
 7 outflow plume and coastal upwelling events: physical and optical properties, *J.*
 8 *Geophys. Res.*, 106(C6), 11613-11622.

9 Kirk, J.T.O. (1994), *Light and phytosynthesis in aquatic ecosystems*, 2nd ed., Cambridge
 10 University Press, New York.

11 Kishino, M., N. Takahashi, N. Okami, and S. Ichimura (1985), Estimation of the spectral
 12 absorption coefficient of phytoplankton in the sea, *Bull. Mar. Sci.*, 37, 634-642.

13 Magnuson, A., L.W. Harding, M.E. Mallonee, and J.E. Adolf (2004), Bio-optical model
 14 for Chesapeake Bay and Middle Atlantic Bight, *Estuar. Coast. Shelf Sci.*, 61, 403-
 15 424.

16 Mannino, A., M.E. Russ, and S.B. Hooker (2008), Algorithm development and validation
 17 for satellite-derived distributions of DOC and CDOM in the U.S. Middle Atlantic
 18 Bight, *J. Geophys. Res.*, doi: 10.1029/2007JC004493, in press.

19 Maritorena, S., D.A. Siegel, and A.R. Peterson (2002), Optimization of a semianalytical
 20 ocean color model for global-scale applications, *Appl. Opt.*, 41, 2705-2714.

21 Marra J., C.C. Trees, and J.E. O'Reilly (2007), Phytoplankton pigment absorption: A
 22 strong predictor of primary productivity in the surface ocean, *Deep Sea Res., Part*
 23 *I*, 54, 155-163.

1 Marshall, H.G., and R.W. Alden (1993), A comparison of phytoplankton assemblages in
2 the Chesapeake and Delaware estuaries (USA), with emphasis on diatoms,
3 *Hydrobiologia*, 269/270, 251-261.

4 Marshall, H.G., and K.K. Nesius (1996), Phytoplankton composition in relation to
5 primary production in Chesapeake Bay, *Mar. Bio.*, 125, 611-617.

6 Marshall, H.G., R.V. Lacouture, C. Buchanan, and J.M. Johnson (2006), Phytoplankton
7 assemblages associated with water quality and salinity regions in Chesapeake
8 Bay, USA, *Estuar. Coast. Shelf Sci.*, 69, 10-18.

9 McClain, C.R., G.C. Feldman, and S.B. Hooker (2004), An overview of the SeaWiFS
10 project and strategies for producing a climate research quality global ocean bio-
11 optical time series, *Deep Sea Res., Part II*, 51, 5-42.

12 Miller, W.D., and L.W. Harding (2007), Climate forcing of the spring bloom in
13 Chesapeake Bay, *Mar. Ecol. Prog. Ser.*, 331, 11-22.

14 Mitchell, B.G. (1990), Algorithms for determining the absorption coefficient of aquatic
15 particulates using the quantitative filter technique (QFT), *Ocean Optics X*, 137-
16 148.

17 Mitchell, B.G., M. Kahru, J. Wieland, and M. Stramska (2002), Determination of spectral
18 absorption coefficients of particles, dissolved material and phytoplankton for
19 discrete water samples, in *Ocean optics protocols for satellite ocean color sensor*
20 *validation, Revision 3*, Vol. 2, edited by J.L. Mueller and G.S. Fargion, pp. 231-
21 257, NASA Goddard Space Flight Center, Greenbelt, Maryland.

22 Mobley, C. (1994), *Light and Water: Radiative Transfer in Natural Waters*, 592 pp.,
23 Academic Press, San Diego, California.

- 1 Mueller, J.L. (2000), SeaWiFS algorithm for the diffuse attenuation coefficient, K(490),
2 using water-leaving radiances at 490 and 555 nm, in O'Reilly, J.E. and co-authors:
3 *SeaWiFS Postlaunch Calibration and Validation Analyses*, Part 3, edited by S.B.
4 Hooker and E.R. Firestone, NASA/TM-2000-206892, Vol. 11, NASA Goddard
5 Space Flight Center, Greenbelt, Maryland, 24-27.
- 6 Nelson, N.B., C.A. Carlson, and D.K. Steinberg (2004), Production of chromophoric
7 dissolved organic matter by Sargasso Sea microbes, *Mar. Chem.*, 89, 273-289.
- 8 O'Reilly, J.E., and C. Zetlin (1998), Seasonal, horizontal, and vertical distribution of
9 phytoplankton chlorophyll a in the northeast U.S. continental shelf ecosystem,
10 *NOAA Technical Report NMFS 139*, 120 pp., U.S. Department of Commerce,
11 Seattle, Washington.
- 12 O'Reilly, J.E., S. Maritorena, B.G. Mitchell, D.A. Siegel, K.L. Carder, S.A. Garver, M.
13 Kahru, and C. McClain (1998), Ocean color algorithms for SeaWiFS. *J. Geophys.*
14 *Res.*, 103, 24937-24953.
- 15 O'Reilly, J.E., et al. (2000), SeaWiFS Postlaunch Calibration and Validation Analyses,
16 Part 3, in Hooker, S.B., Firestone, E.R. (Eds.), *SeaWiFS Post-launch Technical*
17 *Report Series*. NASA Tech. Memo. 2000-206892, vol. 11, NASA Goddard Space
18 Flight Center, Greenbelt, Maryland.
- 19 Paerl, H.W., L.M. Valdes, B.L. Peierls, J.E. Adolf, and L.W. Harding (2006),
20 Anthropogenic and climatic influences on the eutrophication of large estuarine
21 ecosystems, *Limnol. Oceanogr.*, 51(1, part 2), 448-462.
- 22 Pope, R.M., and E.S. Fry (1997), Absorption spectrum (380-700nm) of pure water, II,
23 Integrating cavity measurements, *Appl. Opt.*, 36, 8710-8723.

1 Prieur, L., and S. Sathyendranath (1981), An optical classification of coastal and oceanic
2 waters based on the specific spectral absorption curves of phytoplankton
3 pigments, dissolved organic-matter, and other particulate materials, *Limnol.*
4 *Oceanogr.*, 26, 671-689.

5 Rennie, S.E., J.L. Largier, and S.J. Lentz (1999), Observation of a pulsed buoyancy
6 current downstream of Chesapeake Bay, *J. Geophys. Res.*, 104(C8), 18227-18240.

7 Rochelle-Newall, E.J., and T.R. Fisher (2002), Production of chromophoric dissolved
8 organic matter fluorescence in marine and estuarine environments: an
9 investigation into the role of phytoplankton, *Mar. Chem.*, 77, 7-21.

10 Sanders, T.M., and R.W. Garvine (2001), Fresh water delivery to the continental shelf
11 and subsequent mixing: An observational study, *J. Geophys. Res.*, 106(C11),
12 27087-27101.

13 Siegel, D.A., M. Wang, S. Maritorena, and W.D. Robinson (2000), Atmospheric
14 correction of satellite ocean-color imagery: the black pixel assumption, *Appl. Opt.*,
15 39, 3582-3591.

16 Siegel, D.A., S. Maritorena, N.B. Nelson, D.A. Hansell, and M. Lorenzi-Kayser (2002),
17 Global distribution and dynamics of colored dissolved and detrital organic
18 materials, *J. Geophys. Res.* 107(C12), 3228, doi:10.1029/2001JC000965.

19 Siegel, D.A., S. Maritorena., N.B. Nelson, and M.J. Behrenfeld (2005), Independence and
20 interdependencies among global ocean color properties: Reassessing the bio-
21 optical assumption, *J. Geophys. Res.*, 110(C07011), doi:10.1029/2004JC002527.

22 Signorini, S.R., C.R. McClain, A. Mannino, and S. Bailey (2005), *Report on ocean color*
23 *and carbon study for the south Atlantic Bight and Chesapeake Bay regions,*

1 *NASA/TM-2005-212787*, NASA Goddard Space Flight Center, Greenbelt,
2 Maryland.

3 Steinberg, D.K., N.B. Nelson, C.A. Carlson, and A.C. Prusak (2004), Production of
4 chromophoric dissolved organic matter (CDOM) in the open ocean by
5 zooplankton and the colonial cyanobacterium *Trichodesmium* spp., *Mar. Ecol.*
6 *Prog. Ser.*, 267, 45-56.

7 Trees, C.C., D.K. Clark, R.R. Bidigare, M.E. Ondrusek, and J.L. Mueller (2000),
8 Accessory pigments versus chlorophyll a concentration with the euphotic zone: A
9 ubiquitous relationship, *Limnol. Oceanogr.* 45(5), 1190-1143.

10 Van Heukelem, L., and C.S. Thomas (2001), Computer-assisted high-performance liquid
11 chromatography method development with applications to the isolation and
12 analysis of phytoplankton pigments, *J. Chrom. A*, 910, 31-49.

13 Verity, P.G., J.E. Bauer, C.N. Flagg, D.J. DeMaster, and D. J. Repeta (2002), The Ocean
14 Margins Program: an interdisciplinary study of carbon sources, transformations,
15 and sinks in a temperate continental margin system, *Deep Sea Res., Part II*, 49,
16 4273-4295.

1 Figure captions

2

3 Figure 1. Map of the study area within the southern Middle Atlantic Bight (SMAB).

4 Symbols representing the sampling stations from the following cruises are: \triangle – BIOME1

5 (30 March to 1 April 2005), ∇ – BIOME2 (26 to 30 July 2005), \circ – BIOME3 (5 to 9

6 May 2006), \times – BIOME4 (2 to 6 July 2006), \square – CBP (four daily cruises), and \blacksquare –

7 CBH (ten daily cruises).

8

9 Figure 2. Log-transformed linear regression of phytoplankton absorption coefficient at

10 670 nm [$a_{ph}(670)$] to a) $a_{ph}(443)$, and b) chlorophyll a concentration [Chl a]. The solid

11 and dashed lines in the upper figure represent the regression for summer-fall season (May

12 to October) and winter-spring season (November to April), respectively.

13

14 Figure 3. Absorption algorithms derived from field observations of remote sensing

15 reflectance (R_{rs}) from a) log_linear_model for $a_{ph}(670)$: $\log[a_{ph}(\lambda)] = C_0(\lambda) + C_1(\lambda)R$,

16 where $R = \log[R_{rs}(\lambda_1)/R_{rs}(\lambda_2)]$; and b) log_polynomial_model for non-pigmented

17 particulate absorption coefficient at 380 nm [$a_d(380)$]:

18 $\log[a_d(\lambda)] = D_0(\lambda) + D_1(\lambda)R + D_2(\lambda)R^2 + D_3(\lambda)R^3 + D_4(\lambda)R^4$; and c)

19 exponential_model for CDOM absorption coefficient at 380 nm [$a_g(380)$]:

20 $a_g(\lambda) = G_0(\lambda) + G_1(\lambda)\exp[-G_2(\lambda)\frac{R_{rs}(\lambda_1)}{R_{rs}(\lambda_2)}]$; and d) reverse_exponential_model for

21 absorption coefficient by non-pigmented particles plus CDOM at 380 nm [$a_{dg}(380)$]

1 $\frac{R_{rs}(\lambda_1)}{R_{rs}(\lambda_2)} = H_0(\lambda) + H_1(\lambda) \exp[-H_2(\lambda)a_{dg}(\lambda)]$. Regression lines from R_{rs} band ratios of
2 412/555, 443/555, and 490/555 are represented as solid, dotted, and dashed lines,
3 respectively.

4
5 Figure 4. Validation results comparing SeaWiFS observations with field measurements of
6 $a_{ph}(670)$, $a_d(380)$, $a_g(380)$, and $a_{dg}(380)$ from multiple models (log_linear_model,
7 log_polynomial_model, exponential_model, reverse_exponential_model). Figures a) and
8 b) show the mean absolute percent difference (MAPD), while c) and d) show the root
9 mean square error (RMSE) of the validation results within 8 hours and 32 hours of the
10 satellite overpass, respectively. The data from stations applied to develop the algorithms
11 were not included in this analysis. The satellite derived $a_{ph}(670)$ and $a_{dg}(380)$ from
12 GSM01 model [Maritorena *et al.*, 2002] and GSM01-CB model [Magnuson *et al.*, 2004]
13 are also shown for comparison.

14
15 Figure 5. Validation results comparing MODIS-Aqua observations with field
16 measurements of $a_{ph}(670)$, $a_d(380)$, $a_g(380)$, and $a_{dg}(380)$ from multiple models. See
17 Figure 4 for details.

18
19 Figure 6. Comparisons of SeaWiFS and MODIS-Aqua and field observations of the
20 absorption coefficients of a) $a_{ph}(670)$, b) $a_d(380)$, c) $a_g(380)$, and d) $a_{dg}(380)$. The values
21 are plotted on log scale. The satellite derivations of $a_{ph}(670)$, $a_d(380)$, and $a_{dg}(380)$ were
22 from the log_linear_model, while $a_g(380)$ from the reverse_exponential_model. The
23 match-ups procedure is limited to within ± 8 hours, and the data from stations used to

develop algorithms are excluded for validation analyses. The statistical results are based on log-transformation of the data and shown on upper left for SeaWiFS and lower right for MODIS-Aqua. The solid lines represent the 1:1 lines, while dashed lines and dotted lines represent the regression for SeaWiFS and MODIS-Aqua respectively.

Figure 7. Comparisons of SeaWiFS and MODIS-Aqua and field observations of [Chl_a] for satellite overpass window of a) ± 8 hours and b) ± 32 hours. The data from stations used to develop algorithms of a_{ph} are excluded for this analysis. The solid lines represent the 1:1 lines, while dashed lines and dotted lines represent the regression for SeaWiFS and MODIS-Aqua respectively. See Figure 6 for detail.

Figure 8. The distribution of a_{ph} , a_d , and a_g at 443 nm within the SMAB for 5 August and 3 November 2005, and 15 February and 12 May 2006 representing four seasons. The derived images for 5 August 2005 and 15 February 2006 were from MODIS-Aqua, while the other two were from SeaWiFS.

Figure 9. The distribution of the relative percentage of a_{ph} , a_d , and a_g to their sum at 443 nm within the SMAB. See Figure 8 for detail.

Figure 10. The relative percentage of a_{ph} , a_d , and a_g to their sum at 443 nm from field measurements grouped into two regions (near shore region with bottom depth < 20 m, and offshore region with bottom depth ≥ 20 m) within the SMAB.

1 Figure 11. The distribution of [Chl_a] calculated from operational ocean color algorithms
2 (OC4V4 for SeaWiFS and OC3M for MODIS-Aqua) and from the empirical method
3 described in this paper (OC_SMAB; $[Chl_a] = 70.632 \times [a_{ph}(670)]^{1.184}$), and their ratio
4 $[(OC4V4 \text{ or } OC3M)/OC_SMAB]$ within the SMAB. See Figure 8 for detail. The
5 responding scales of the color bar are in log units for [Chl_a] and in linear units for the
6 ratio.

7
8 Figure 12. Monthly time series of a) [Chl_a], b) $a_g(443)$, and c) diffuse attenuation
9 coefficient at 490 nm (K490) from MODIS-Aqua Level-3 images (4x4 km resolution) for
10 a near shore location (75.90W, 36.93N; solid circle) and a middle shelf location (75.30W,
11 36.93N; open circle). [Chl_a] and $a_g(443)$ are calculated from algorithms developed in
12 this paper, while K490 is a direct product from the Level-3 images. Monthly river
13 discharge rates at the mouth of Chesapeake Bay (open triangle; Data sources:
14 <http://waterdata.usgs.gov/nwis/>; written communication from Gary Fisher, U.S.
15 Geological Survey, 17 July 2007) are also shown for comparison.

Table 1. Regression results of phytoplankton absorption coefficient (a_{ph}) to $a_{ph}(670)$ from Equation (3): $a_{ph}(\lambda) = B_0(\lambda)[a_{ph}(670)]^{B_1(\lambda)}$. Log-transformation was applied to the data and Model II linear regression was adopted to calculate $\log[B_0(\lambda)]$ and $B_1(\lambda)$. The selected wavelengths for a_{ph} analysis were the visible bands for SeaWiFS and MODIS-Aqua.

λ (nm)	May-October (N=196)			November-April (N=51)		
	B_0	B_1	r^2	B_0	B_1	r^2
412	1.296	0.835	0.986	1.131	0.849	0.987
443	1.525	0.843	0.989	1.290	0.848	0.979
488	1.023	0.846	0.983	0.806	0.821	0.961
490	1.015	0.851	0.983	0.800	0.825	0.963
510	0.842	0.911	0.983	0.637	0.856	0.975
531	0.694	0.983	0.970	0.489	0.875	0.974
551	0.603	1.047	0.945	0.378	0.893	0.956
555	0.587	1.067	0.938	0.347	0.895	0.948
667	0.899	1.005	1.000	0.923	1.012	1.000
678	1.039	1.002	0.999	0.914	0.959	0.994

Table 2. Statistical results for absorption coefficients of phytoplankton (a_{ph}), non-pigmented particles (a_d), and CDOM plus non-pigmented particles (a_{dg}) at selected wavelengths from log_linear_model: $\log[a_x(\lambda)] = C_0(\lambda) + C_1(\lambda)R$, where $R = \log[R_{rs}(\lambda_1)/R_{rs}(\lambda_2)]$. The size of the dataset is N=25.

Parameter	$R_{rs}(490)/R_{rs}(555)$			$R_{rs}(490)/R_{rs}(551)$		
	C_1	C_0	r^2	C_1	C_0	r^2
$a_{ph}(670)$	-2.602	-1.467	0.921	-2.769	-1.487	0.923
$a_d(380)$	-2.797	-1.319	0.933	-2.976	-1.340	0.932
$a_d(400)$	-2.812	-1.387	0.933	-2.992	-1.408	0.931
$a_d(412)$	-2.849	-1.427	0.933	-3.031	-1.449	0.931
$a_d(443)$	-3.048	-1.633	0.925	-3.243	-1.656	0.924
$a_d(490)$	-3.260	-1.950	0.902	-3.468	-1.975	0.902
$a_d(510)$	-3.584	-2.105	0.864	-3.813	-2.132	0.864
$a_d(531)$	-3.676	-2.223	0.848	-3.911	-2.251	0.848
$a_d(555)$	-3.315	-2.297	0.891	-3.526	-2.322	0.891
$a_{dg}(380)$	-1.394	-0.434	0.919	-1.487	-0.445	0.919
$a_{dg}(400)$	-1.489	-0.576	0.921	-1.588	-0.587	0.920
$a_{dg}(412)$	-1.535	-0.651	0.922	-1.637	-0.663	0.922
$a_{dg}(443)$	-1.593	-0.879	0.923	-1.698	-0.891	0.923
$a_{dg}(490)$	-1.649	-1.190	0.910	-1.758	-1.203	0.910
$a_{dg}(510)$	-1.725	-1.308	0.899	-1.840	-1.322	0.899
$a_{dg}(531)$	-1.633	-1.406	0.885	-1.743	-1.419	0.886
$a_{dg}(555)$	-1.983	-1.564	0.822	-2.117	-1.580	0.823

Table 3. Statistical results for CDOM absorption coefficient (a_g) at selected wavelengths

from the reverse_exponential_model: $\frac{R_{rs}(\lambda_1)}{R_{rs}(\lambda_2)} = H_0(\lambda) + H_1(\lambda) \exp[-H_2(\lambda)a_g(\lambda)]$. The

size of the dataset is N=34.

Parameter	$R_{rs}(490)/R_{rs}(555)$				$R_{rs}(490)/R_{rs}(551)$			
	H_0	H_1	H_2	r^2	H_0	H_1	H_2	r^2
$a_g(355)$	0.538	3.149	3.978	0.882	0.546	2.805	3.844	0.879
$a_g(380)$	0.534	3.015	6.110	0.902	0.542	2.692	5.909	0.900
$a_g(400)$	0.540	2.940	8.656	0.915	0.547	2.625	8.366	0.912
$a_g(412)$	0.523	2.849	9.914	0.916	0.531	2.551	9.592	0.914
$a_g(443)$	0.531	2.857	17.700	0.908	0.539	2.557	17.130	0.906
$a_g(490)$	0.547	3.138	39.960	0.891	0.555	2.798	38.690	0.890
$a_g(510)$	0.493	2.352	39.870	0.857	0.503	2.126	38.640	0.858
$a_g(531)$	0.494	2.271	50.240	0.829	0.504	2.056	48.700	0.831
$a_g(555)$	0.335	1.798	40.690	0.795	0.346	1.657	39.120	0.799

Table 4. The mean absolute percent difference (MAPD) and root mean square error (RMSE) from validation match-ups for a_{ph} , a_d , a_g , and a_{dg} at selected wavelengths. The derived exponential decay slope (S) for a_d (S_d), a_g (S_g), and a_{dg} (S_{dg}) from non-linear regression and chlorophyll a concentration ([Chl_a]) are also compared. Data used for algorithm development are not included in this analysis. The size of the datasets are N=22, 36, 8, and 19 for a_{ph} , a_d , or a_{dg} , and N=29, 45, 14, and 25 for [Chl_a], and N=31, 47, 14, and 25 for a_g for SeaWiFS ± 8 and ± 32 hours and MODIS ± 8 and ± 32 hours overpass windows, respectively.

Parameter	SeaWiFS ($\pm 8h$)		SeaWiFS ($\pm 32h$)		MODIS ($\pm 8h$)		MODIS ($\pm 32h$)	
	MAPD	RMSE	MAPD	RMSE	MAPD	RMSE	MAPD	RMSE
$a_{ph}(443)$	23.5	0.0501	23.4	0.0470	23.4	0.0137	23.1	0.0206
$a_{ph}(670)$	25.7	0.0371	30.1	0.0329	21.2	0.0051	27.8	0.0106
[Chl_a]	32.3	3.6808	32.5	3.0339	28.8	3.2805	29.3	2.5474
$a_d(380)$	35.3	0.1447	38.2	0.1350	41.9	0.1684	39.3	0.1275
$a_d(443)$	41.8	0.0787	42.1	0.0726	50.5	0.0876	44.6	0.0664
S_d	13.4	0.0018	11.7	0.0016	11.5	0.0014	12.1	0.0015
$a_g(380)$	25.2	0.1636	20.7	0.1359	20.1	0.2096	23.4	0.1607
$a_g(443)$	22.8	0.0516	20.1	0.0432	20.1	0.0662	21.5	0.0509
S_g	5.8	0.0011	5.5	0.0011	5.2	0.0011	6.7	0.0012
$a_{dg}(380)$	26.5	0.2104	25.2	0.1965	18.4	0.1761	25.6	0.1478
$a_{dg}(443)$	24.4	0.0923	24.4	0.0870	22.1	0.0896	23.1	0.0711
S_{dg}	11.9	0.0020	12.7	0.0021	15.5	0.0024	15.1	0.0023

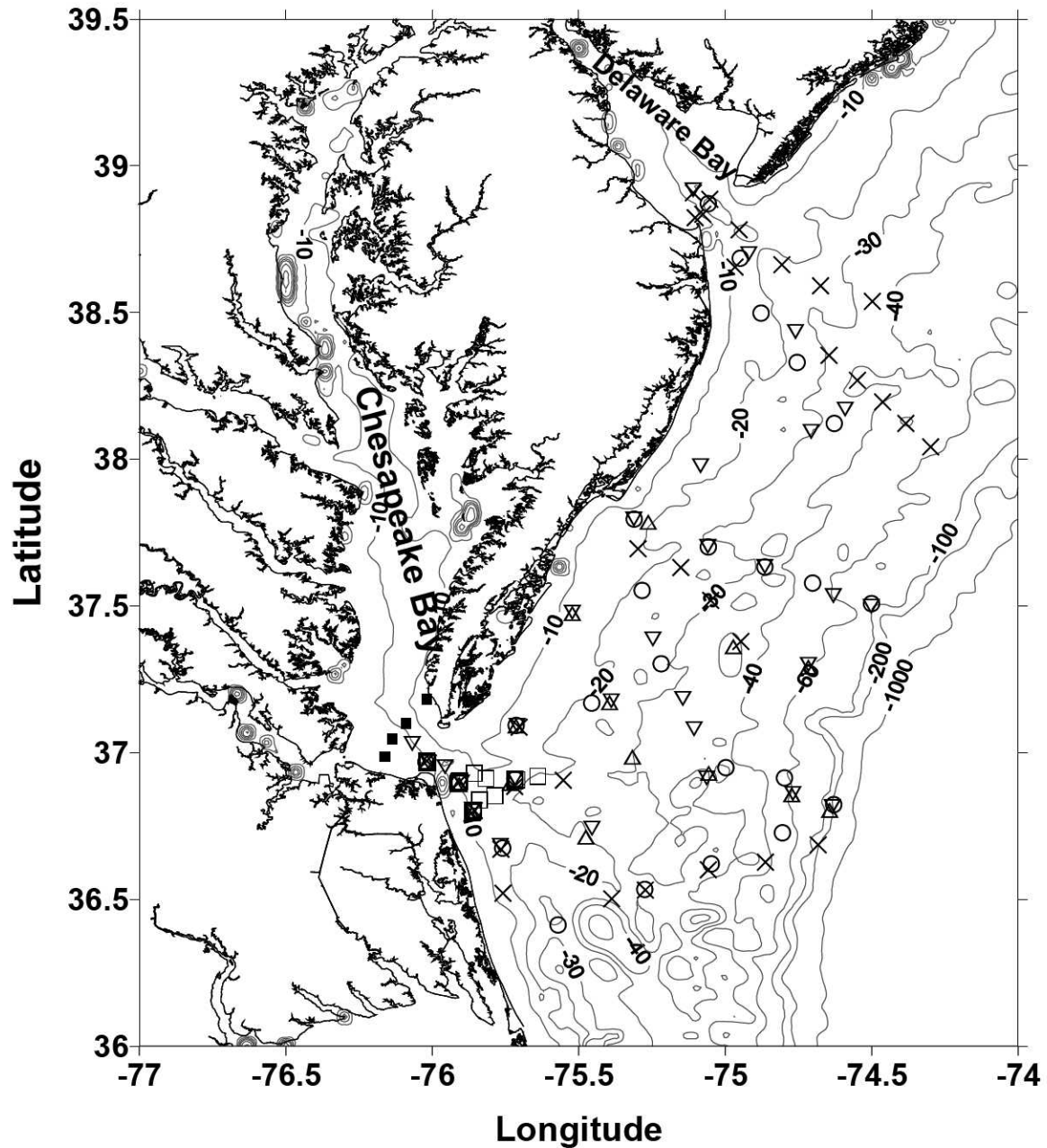


Figure 1. Map of the study area within the southern Middle Atlantic Bight (SMAB).

Symbols representing the sampling stations from the following cruises are: \triangle – BIOME1 (30 March to 1 April 2005), ∇ – BIOME2 (26 to 30 July 2005), \circ – BIOME3 (5 to 9 May 2006), \times – BIOME4 (2 to 6 July 2006), \square – CBP (four daily cruises), and \blacksquare – CBH (ten daily cruises).

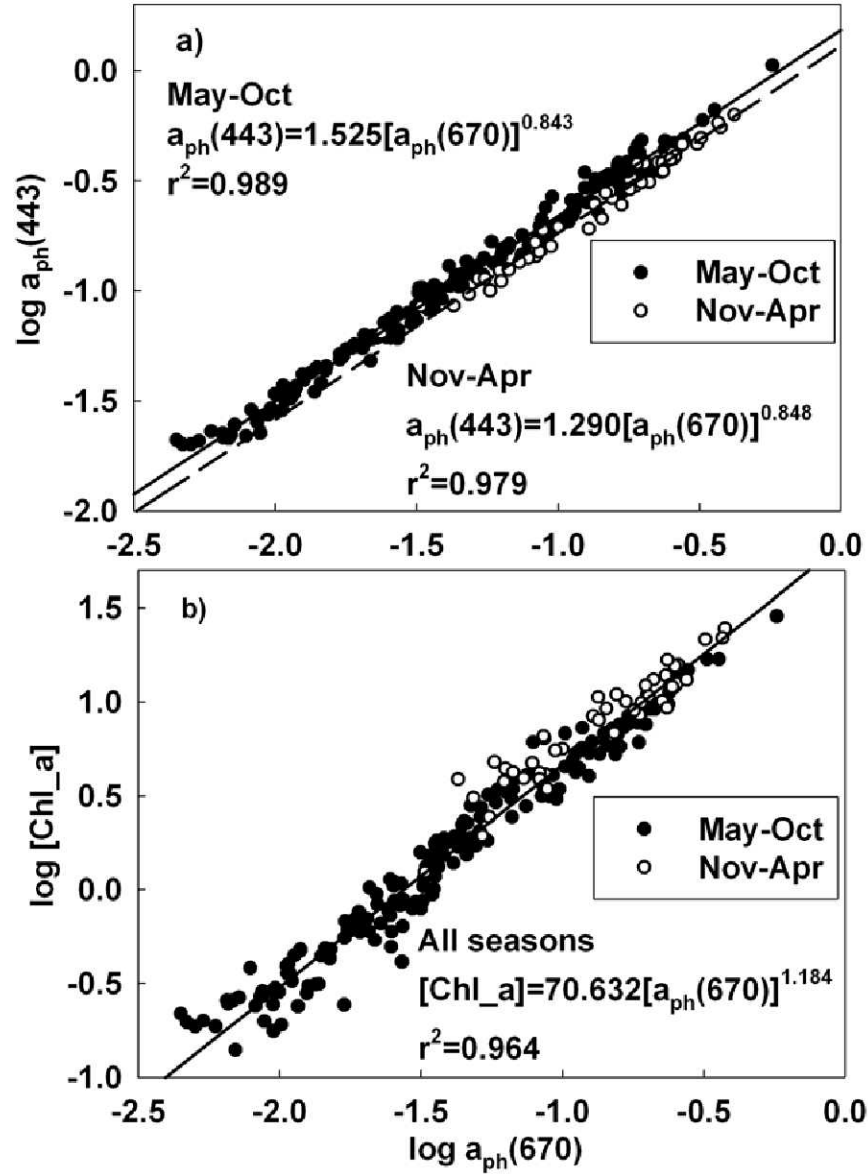


Figure 2. Log-transformed linear regression of phytoplankton absorption coefficient at 670 nm [$a_{ph}(670)$] to a) $a_{ph}(443)$, and b) chlorophyll *a* concentration [Chl_a]. The solid and dashed lines in the upper figure represent the regression for summer-fall season (May to October) and winter-spring season (November to April), respectively.

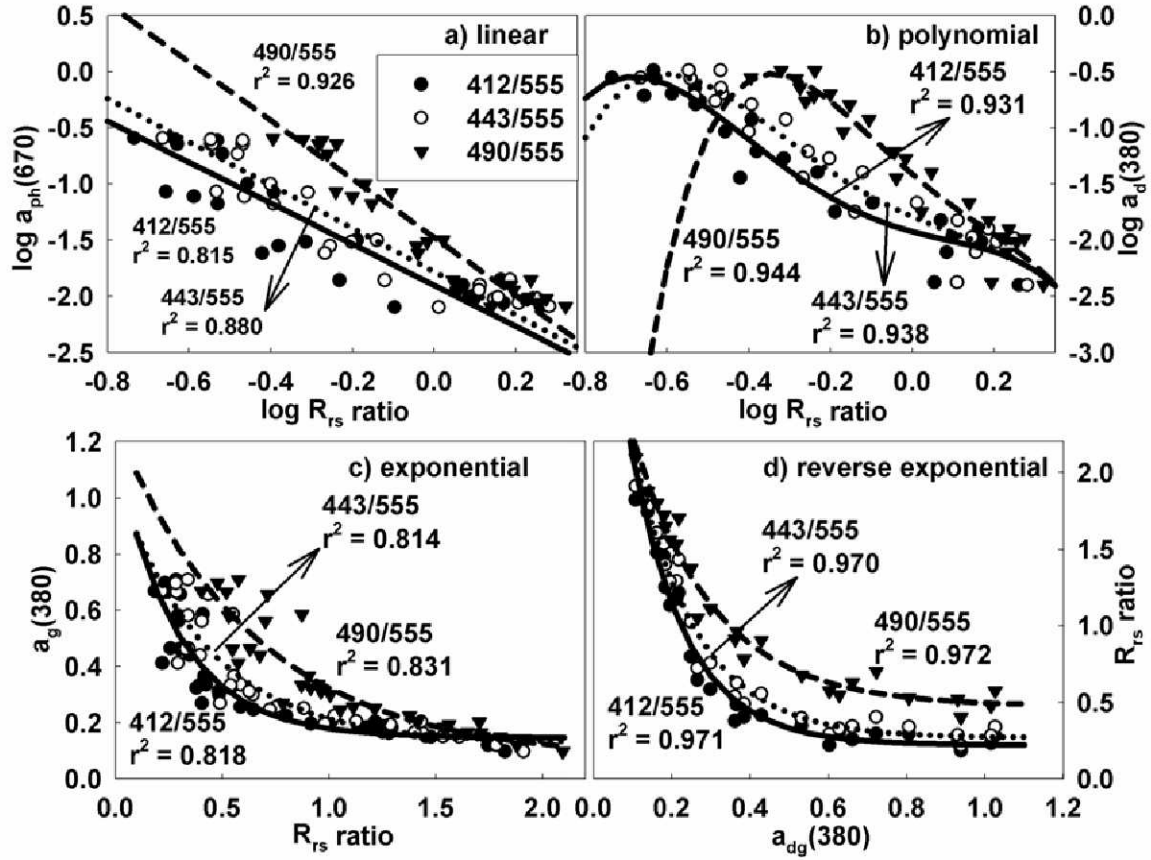


Figure 3. Absorption algorithms derived from field observations of remote sensing reflectance (R_{rs}) from a) log_linear_model for $a_{ph}(670)$: $\log[a_{ph}(\lambda)] = C_0(\lambda) + C_1(\lambda)R$, where $R = \log[R_{rs}(\lambda_1)/R_{rs}(\lambda_2)]$; and b) log_polynomial_model for non-pigmented particulate absorption coefficient at 380 nm [$a_d(380)$]:

$\log[a_d(\lambda)] = D_0(\lambda) + D_1(\lambda)R + D_2(\lambda)R^2 + D_3(\lambda)R^3 + D_4(\lambda)R^4$; and c)

exponential_model for CDOM absorption coefficient at 380 nm [$a_g(380)$]:

$$a_g(\lambda) = G_0(\lambda) + G_1(\lambda) \exp[-G_2(\lambda) \frac{R_{rs}(\lambda_1)}{R_{rs}(\lambda_2)}]; \text{ and d) reverse_exponential_model for}$$

absorption coefficient by non-pigmented particles plus CDOM at 380 nm [$a_{dg}(380)$]

$$\frac{R_{rs}(\lambda_1)}{R_{rs}(\lambda_2)} = H_0(\lambda) + H_1(\lambda) \exp[-H_2(\lambda)a_{dg}(\lambda)]. \text{ Regression lines from } R_{rs} \text{ band ratios of}$$

412/555, 443/555, and 490/555 are represented as solid, dotted, and dashed lines, respectively.

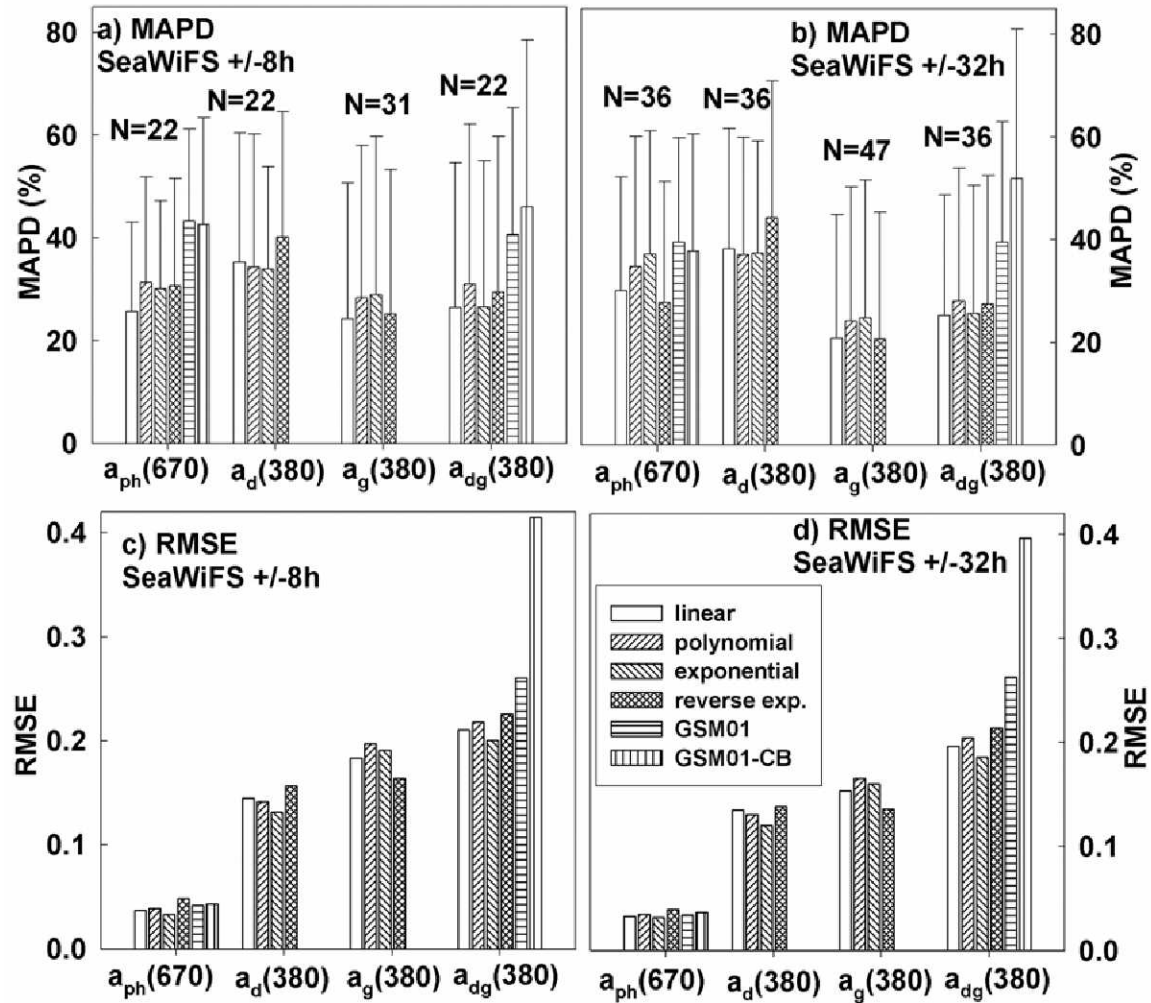


Figure 4. Validation results comparing SeaWiFS observations with field measurements of $a_{ph}(670)$, $a_d(380)$, $a_g(380)$, and $a_{dg}(380)$ from multiple models (log_linear_model, log_polynomial_model, exponential_model, reverse_exponential_model). Figures a) and b) show the mean absolute percent difference (MAPD), while c) and d) show the root mean square error (RMSE) of the validation results within 8 hours and 32 hours of the satellite overpass, respectively. The data from stations applied to develop the algorithms were not included in this analysis. The satellite derived $a_{ph}(670)$ and $a_{dg}(380)$ from GSM01 model [Maritorena et al., 2002] and GSM01-CB model [Magnuson et al., 2004] are also shown for comparison.

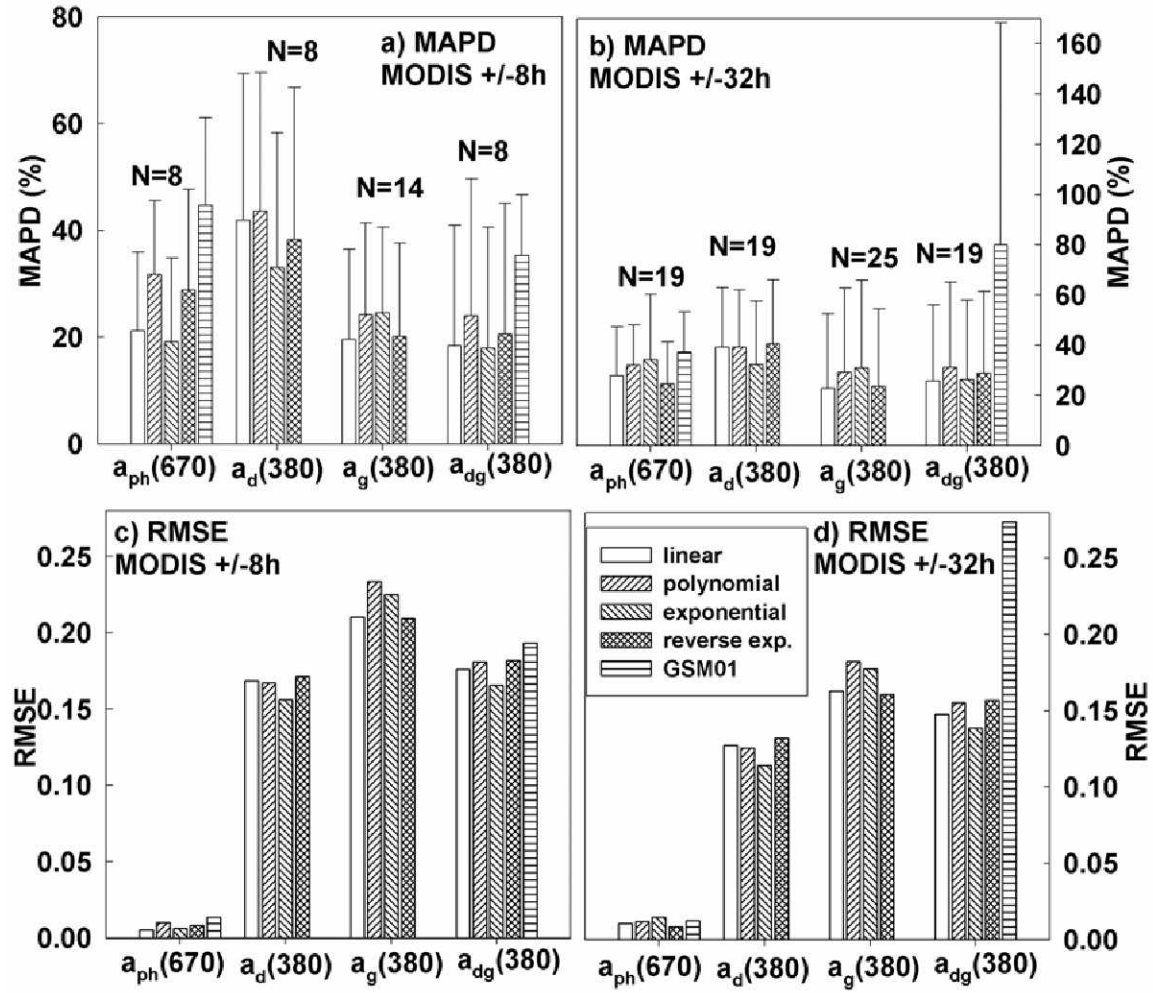


Figure 5. Validation results comparing MODIS-Aqua observations with field measurements of $a_{ph}(670)$, $a_d(380)$, $a_g(380)$, and $a_{dg}(380)$ from multiple models. See Figure 4 for details.

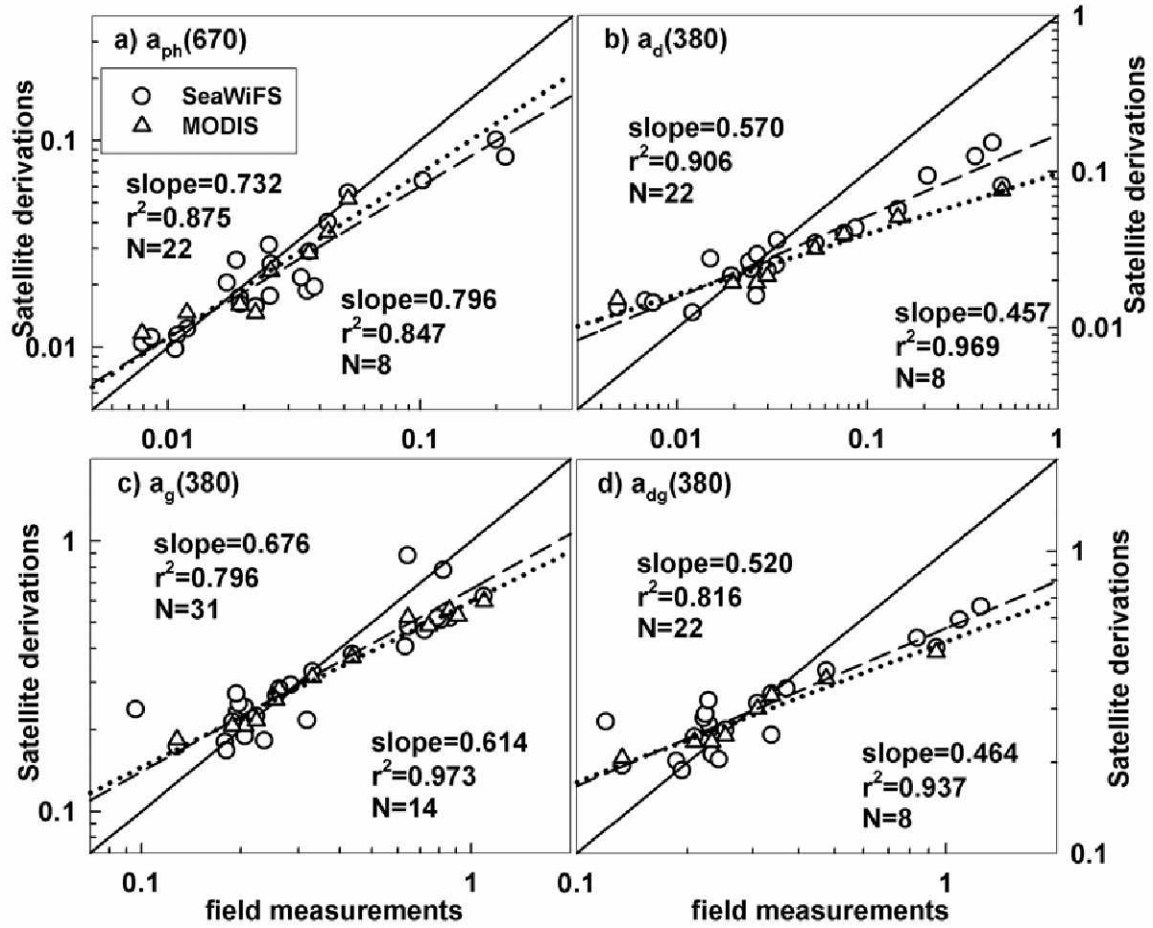


Figure 6. Comparisons of SeaWiFS and MODIS-Aqua and field observations of the absorption coefficients of a) $a_{ph}(670)$, b) $a_d(380)$, c) $a_g(380)$, and d) $a_{dg}(380)$. The values are plotted on log scale. The satellite derivations of $a_{ph}(670)$, $a_d(380)$, and $a_{dg}(380)$ were from the log_linear_model, while $a_g(380)$ from the reverse_exponential_model. The match-ups procedure is limited to within ± 8 hours, and the data from stations used to develop algorithms are excluded for validation analyses. The statistical results are based on log-transformation of the data and shown on upper left for SeaWiFS and lower right for MODIS-Aqua. The solid lines represent the 1:1 lines, while dashed lines and dotted lines represent the regression for SeaWiFS and MODIS-Aqua respectively.

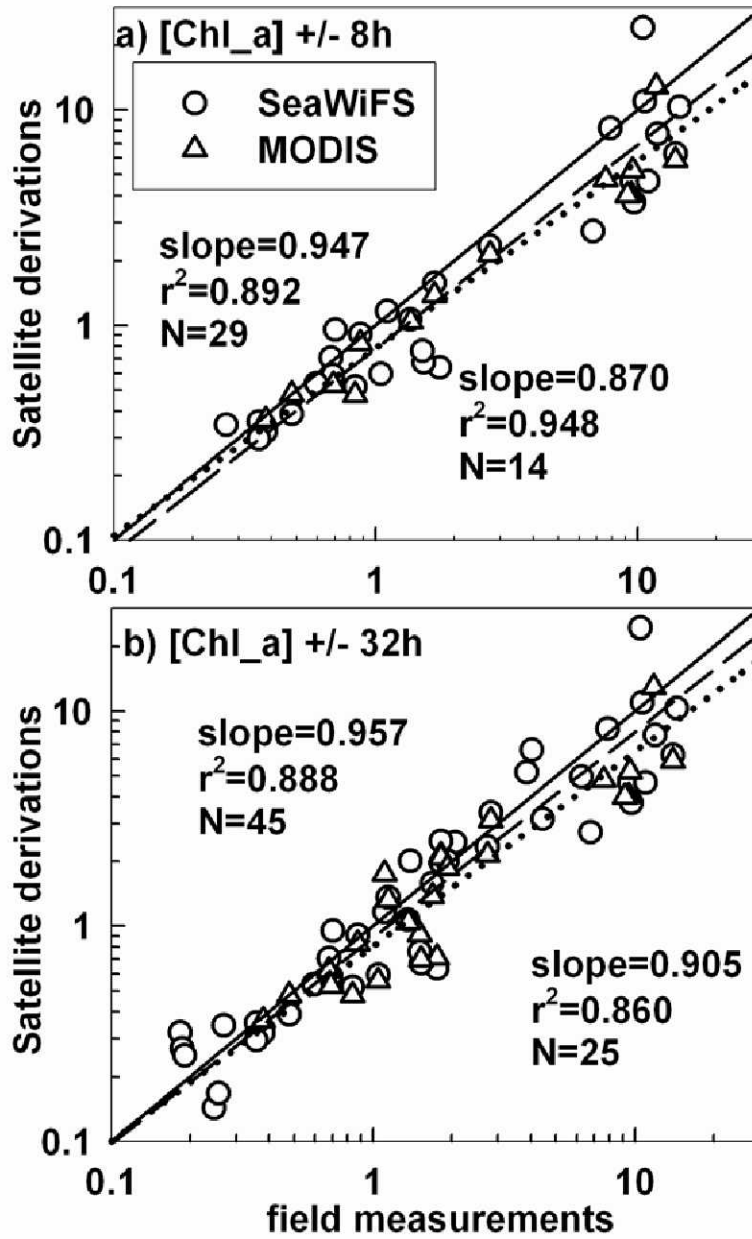


Figure 7. Comparisons of SeaWiFS and MODIS-Aqua and field observations of [Chl_a] for satellite overpass window of a) ± 8 hours and b) ± 32 hours. The data from stations used to develop algorithms of a_{ph} are excluded for this analysis. The solid lines represent the 1:1 lines, while dashed lines and dotted lines represent the regression for SeaWiFS and MODIS-Aqua respectively. See Figure 6 for detail.

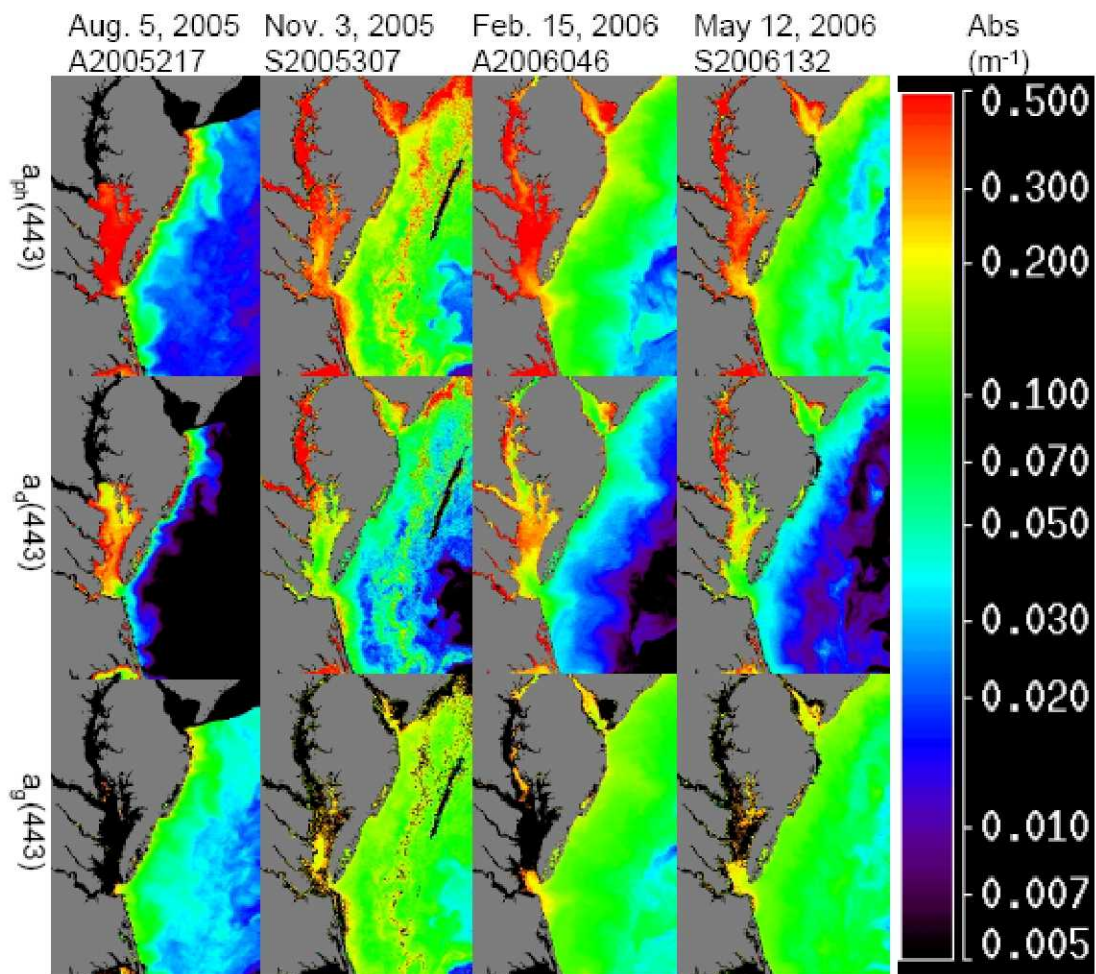


Figure 8. The distribution of a_{ph} , a_d , and a_g at 443 nm within the SMAB for 5 August and 3 November 2005, and 15 February and 12 May 2006 representing four seasons. The derived images for 5 August 2005 and 15 February 2006 were from MODIS-Aqua, while the other two were from SeaWiFS.

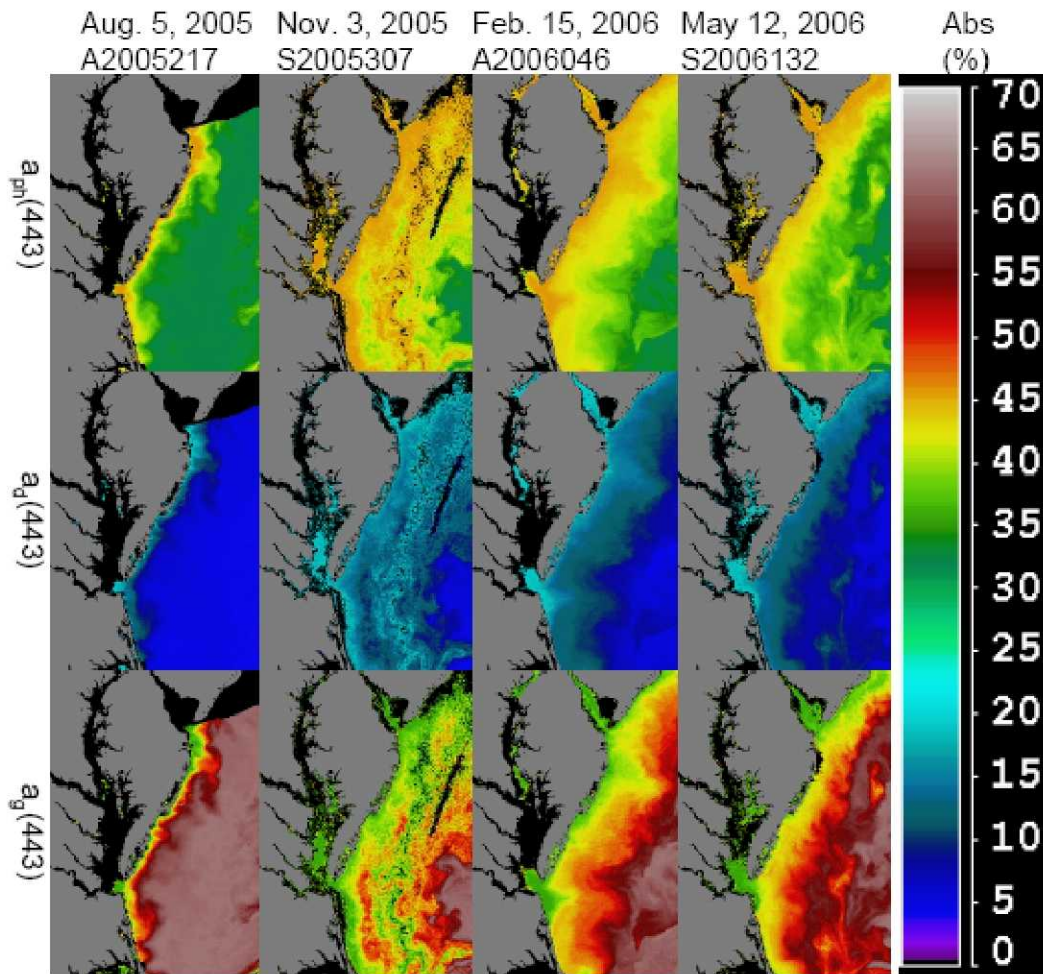


Figure 9. The distribution of the relative percentage of a_{ph} , a_d , and a_g to their sum at 443 nm within the SMAB. See Figure 8 for detail.

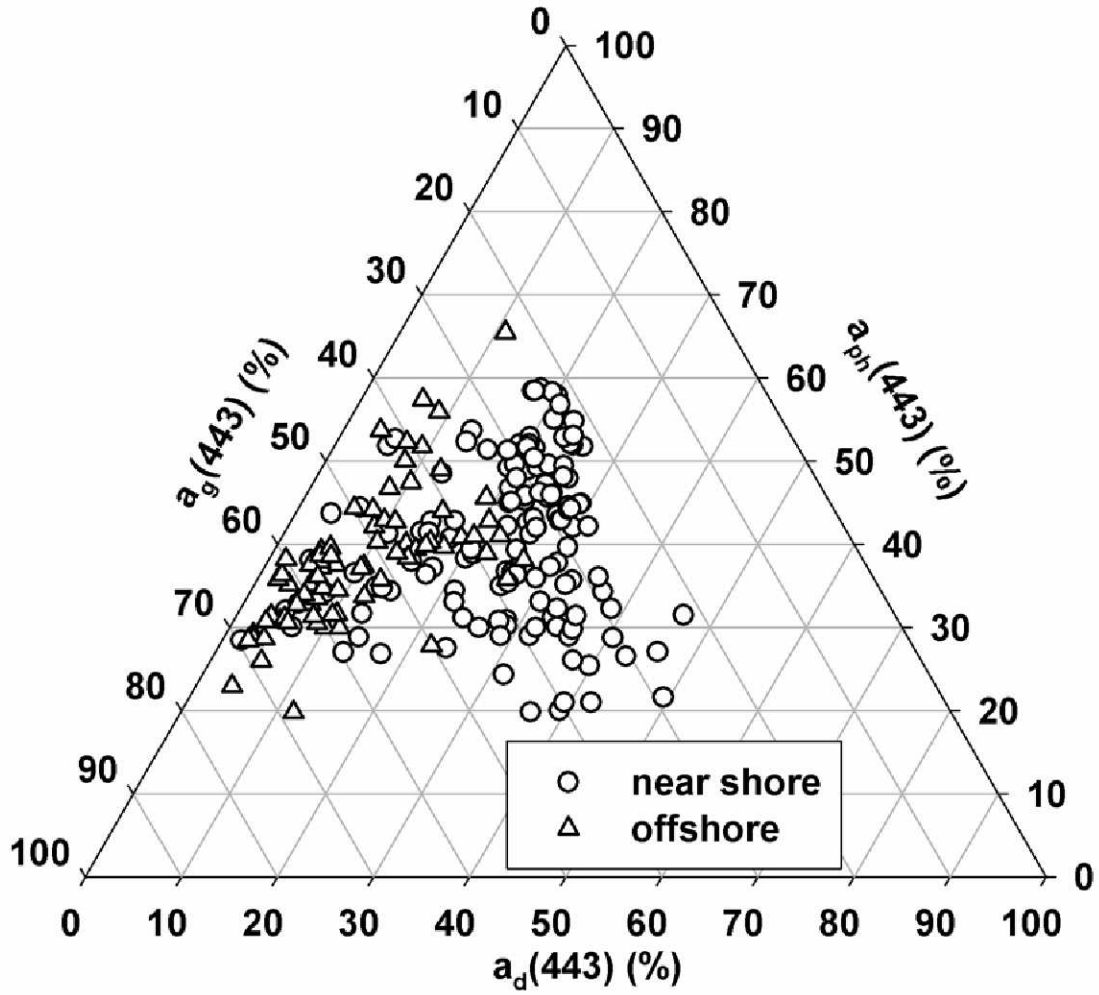


Figure 10. The relative percentage of a_{ph} , a_d , and a_g to their sum at 443 nm from field measurements grouped into two regions (near shore region with bottom depth <20 m, and offshore region with bottom depth ≥ 20 m) within the SMAB.

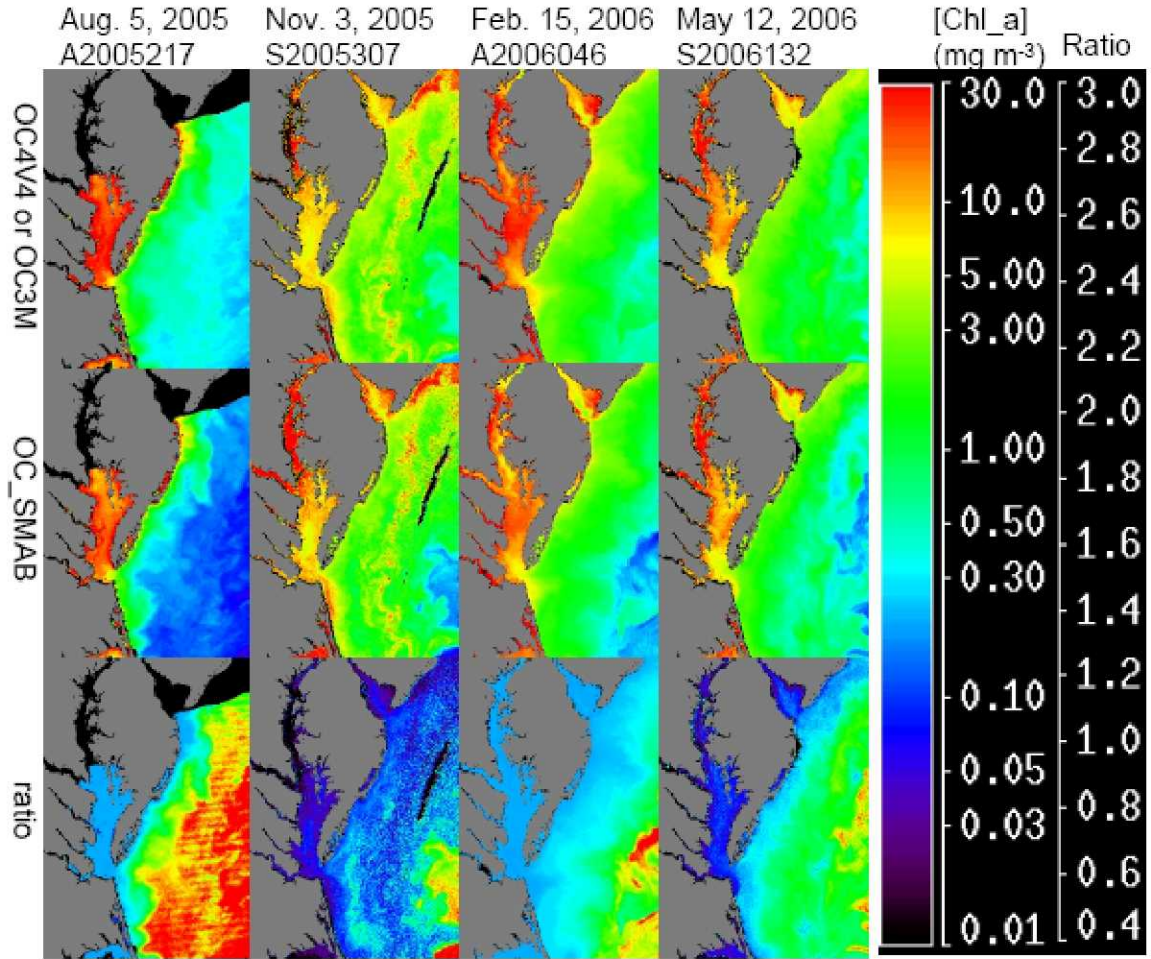


Figure 11. The distribution of [Chl_a] calculated from operational ocean color algorithms (OC4V4 for SeaWiFS and OC3M for MODIS-Aqua) and from the empirical method described in this paper (OC_SMAB; $[Chl_a] = 70.632 \times [a_{ph}(670)]^{1.184}$), and their ratio $[(OC4V4 \text{ or } OC3M)/OC_SMAB]$ within the SMAB. See Figure 8 for detail. The responding scales of the color bar are in log units for [Chl_a] and in linear units for the ratio.

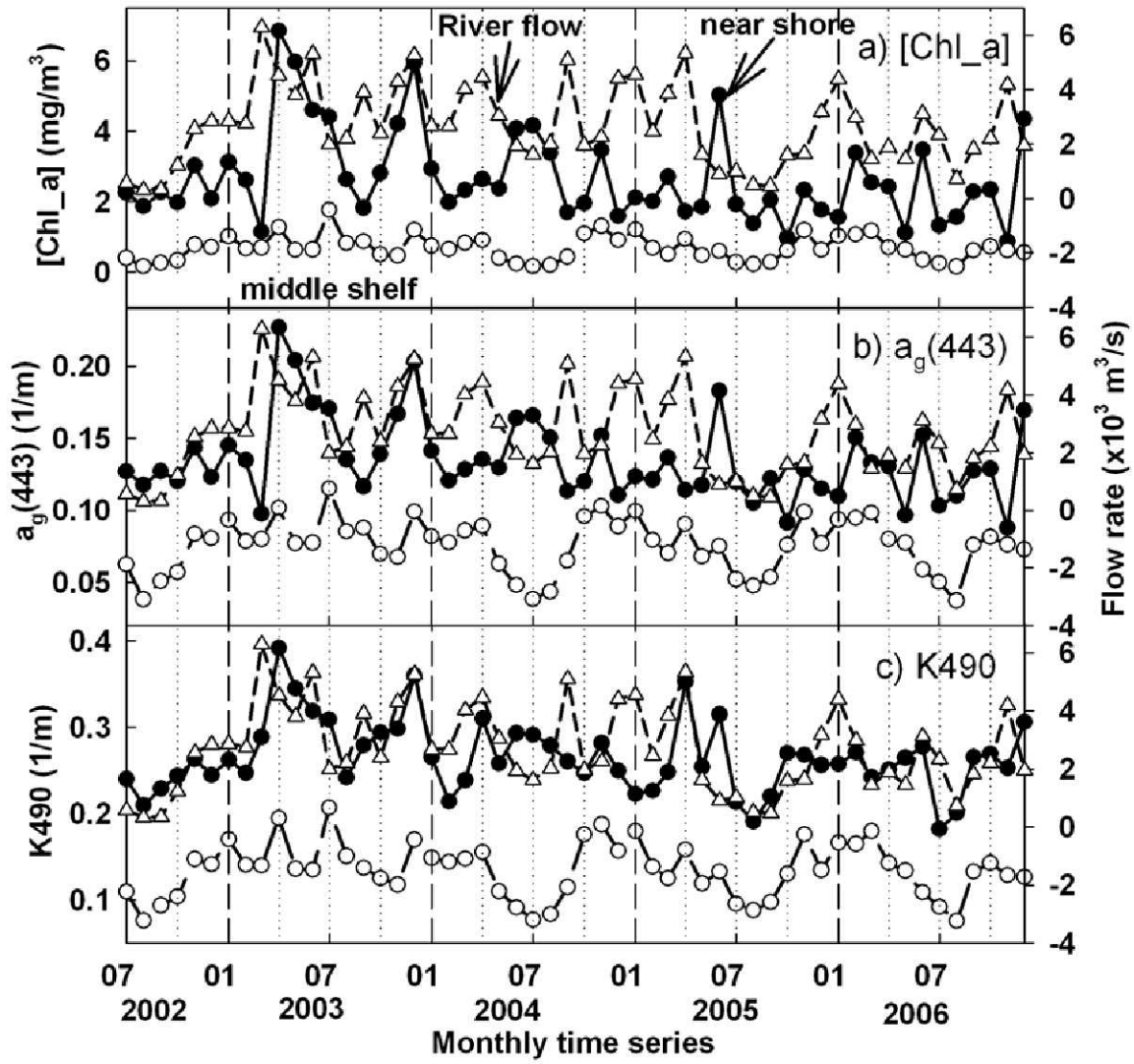


Figure 12. Monthly time series of a) $[Chl_a]$, b) $a_g(443)$, and c) diffuse attenuation coefficient at 490 nm (K490) from MODIS-Aqua Level-3 images (4x4 km resolution) for a near shore location (75.90W, 36.93N; solid circle) and a middle shelf location (75.30W, 36.93N; open circle). $[Chl_a]$ and $a_g(443)$ are calculated from algorithms developed in this paper, while K490 is a direct product from the Level-3 images. Monthly river discharge rates at the mouth of Chesapeake Bay (open triangle; Data sources: <http://waterdata.usgs.gov/nwis/>; written communication from Gary Fisher, U.S. Geological Survey, 17 July 2007) are also shown for comparison.